Eur. Phys. J. E (2011) **34**: 113
DOI 10.1140/epje/i2011-11113-9

THE EUROPEAN PHYSICAL JOURNAL E

Regular Article

Lubricated sliding dynamics: Flow factors and Stribeck curve

B.N.J. Persson[1,a,b] and M. Scaraggi[2]

[1] IFF, FZ Jülich, D-52425 Jülich, Germany
[2] DIMeG-Politecnico di Bari, V. le Japigia 182, 70126 Bari, Italy

Received 5 June 2011 and Received in final form 16 August 2011
Published online: 20 October 2011 –

Abstract. We study the fluid flow at the interface between elastic solids with randomly rough surfaces. We derive (approximate) analytical expressions for the fluid flow factors which enter in the equation describing the fluid flow, and for the frictional shear stress factors which enter in the equation for the frictional shear stress. Numerical results for a rubber cylinder with surface roughness sliding on a flat lubricated substrate, under "low" and "high" pressure conditions, are presented and discussed. Finally we discuss the role of the fluid-induced elastic deformations of the surface roughness profile.

1 Introduction

The influence of surface roughness on fluid flow at the interface between solids in stationary or sliding contact is a topic of great importance both in nature and technology. Technological applications includes leakage of seals, mixed lubrication, and removal of water from the tire-road footprint. In nature fluid removal (squeeze-out) is important for adhesion and grip between the tree frog or Gecko adhesive toe pads and the countersurface during raining, and for cell adhesion.

Almost all surfaces in nature and most surfaces of interest in tribology have roughness on many different length scales, sometimes extending from atomic distances ($\sim$ 1 nm) to the macroscopic size of the system which could be of order $\sim$ 1 cm. Often the roughness is fractal-like so that when a small region is magnified (in general with different magnification in the parallel and orthogonal directions) it "looks the same" as the unmagnified surface.

Most objects produced in engineering have some particular macroscopic shape characterized by a radius of curvature (which may vary over the surface of the solid) *e.g.*, the radius R of a cylinder in a combustion engine. In this case the surface may appear perfectly smooth to the naked eye but at short enough length scale, in general much smaller than R, the surface will exhibit strong irregularities (surface roughness). The surface roughness power spectrum $C(\mathbf{q})$ of such a surface will exhibit a roll-off wavelength $\lambda_0 \ll R$ (related to the roll-off wave vector $q_0 = 2\pi/\lambda_0$) and will appear smooth (except for the macroscopic curvature R) on length scales much larger than λ_0. In this case, when studying the fluid flow between two macroscopic solids, one may homogenize the microscopic fluid dynamics occurring at the interface, resulting in effective fluid flow equations describing the average fluid flow on length scales much larger than λ_0, and which can be used to study, *e.g.*, the lubrication of the cylinder in an engine. This approach of eliminating or integrating out short length scale degrees of freedom to obtain effective equations of motion which describes the long distance (or slow) behavior is a very general and powerful concept often used in physics.

In the context of fluid flow at the interface between closely spaced solids with surface roughness, Patir and Cheng [1,2] have shown how the Navier-Stokes equations of fluid dynamics can be reduced to effective equations of motion involving locally averaged fluid pressure and flow velocities. In the effective lubrication equation the so called flow factors occur, which are functions of the locally averaged interfacial separation $\bar{u}$. They showed how the flow factors can be determined by solving numerically the fluid flow in small rectangular units with linear size of order of (or larger than) the roll-off wavelength λ_0 introduced above, and by averaging over several realizations. However, with the present speed (and memory) computational limits fully converged solutions using this approach can only take into account roughness over two or at most three decades in length scale. In addition, Patir and Cheng did not include the long-range elastic deformations of the solid walls in the analysis. Later studies have somehow attempted to include elastic deformation using the contact mechanics model of Greenwood-Williamson (GW) [3], but it is now known that this theory (and other asperity contact models [4]) does not correctly describe contact mechanics because of the neglect of the long-range elastic coupling between the asperity contact regions [5,6].

[a] e-mail: b.persson@fz-juelich.de
[b] www.MultiscaleConsulting.com

In particular, the relation between the average interfacial separation $\bar{u}$ and the squeezing pressure p, which is very important for the fluid flow problem, is incorrectly described by the GW model [7–9].

Patir and Cheng's research activity was followed by many other studies on how to eliminate or integrate out the surface roughness in fluid flow problems (see, *e.g.*, refs. [10–12]). Most of these theories involves solving numerically for the fluid flow in rectangular interfacial units and, just as in the Patir and Cheng approach, cannot include roughness on more than ~ 2 decades in length scale. In addition, in some of the studies the measured roughness topography must be "processed" in a non-trivial way in order to obey periodic boundary conditions (which is necessary for the Fast Fourier Transform method used in some of these studies).

Tripp [13] has presented an analytical derivation of the flow factors for the case where the separation between the surfaces is so large that no direct solid-solid contact occurs. He obtained the flow factors to first order in $\langle h^2\rangle/\bar{u}^2$, where $\langle h^2\rangle$ is the ensemble average of the square of the roughness amplitude and $\bar{u}$ the average surface separation. The result of Tripp has recently been generalized to include elastic deformations of the solids [14, 16].

Many surfaces of practical importance have roughness with isotropic statistical properties, *e.g.*, sandblasted surfaces or surfaces coated with particles typically bound by a resin to an otherwise flat surface, *e.g.*, sandpaper surfaces. However some surfaces of engineering interest have surface roughness with anisotropic statistical properties, *e.g.*, surfaces which have been polished or grinded in one direction. The theories of Patir and Chen [1, 2] and of Tripp [13] can be applied also to surfaces with anisotropic statistical properties. The surface anisotropy is often characterized by a single number, the so-called Peklenik number γ, which is the ratio between the decay length ξ_x and ξ_y of the height-height correlation function $\langle h(x,y)h(0,0)\rangle$ along the x- and y-directions, respectively, *i.e.* $\gamma = \xi_x/\xi_y$. Here it has been assumed that the x-axis is oriented along one of the principal direction of the anisotropic surface roughness.

In this paper we present a new approach to calculate the fluid flow at the interface between two elastic solids with randomly rough surfaces. We derive analytical expressions for the fluid pressure and shear flow factors, $\phi_{\rm p}$ and $\phi_{\rm s}$, which enter in the basic equation of fluid flow at interfaces, and the frictional shear stress factors $\phi_{\rm f}$, $\phi_{\rm fs}$ and $\phi_{\rm fp}$, which enter in the expression for the frictional shear stress. We also discuss how lubricant shear thinning can be included in the analysis.

2 Fluid flow between solids with random surface roughness

Consider two elastic solids with randomly rough surfaces. Even if the solids are squeezed in contact, because of the surface roughness there will in general be non-contact regions at the interface and, if the squeezing force is not too large, there will exist non-contact channels from one side to the other side of the nominal contact region. We consider now fluid flow at the interface between the solids. We assume that the fluid is Newtonian and that the fluid velocity field $\mathbf{v}(\mathbf{x},t)$ satisfies the Navier-Stokes equation

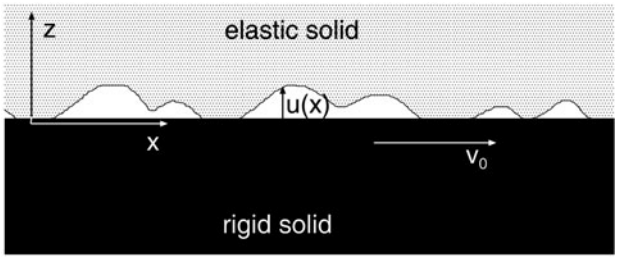

Fig. 1. An elastic solid (block) with a rough surface in contact with a rigid solid (substrate) with a flat surface. The substrate moves with the velocity $\mathbf{v}_0$ while the block is stationary.

$$\frac{\partial \mathbf{v}}{\partial t} + \mathbf{v}\cdot\nabla\mathbf{v} = -\frac{1}{\rho}\nabla p + \nu\nabla^2\mathbf{v},$$

where $\nu = \eta/\rho$ is the kinetic viscosity and ρ the mass density. For simplicity we will also assume an incompressible fluid so that

$$\nabla\cdot\mathbf{v} = 0.$$

We assume that the non-linear term $\mathbf{v}\cdot\nabla\mathbf{v}$ can be neglected (which corresponds to small inertia and small Reynolds number), which is usually the case in fluid flow between narrowly spaced solid walls. For simplicity we assume the lower solid to be rigid with a flat surface, while the upper solid is elastic with a rough surface. We introduce a coordinate system xyz with the xy-plane on the surface of the lower solid and the z-axis pointing towards the upper solid, see fig. 1. The lower solid moves with the velocity $\mathbf{v}_0$ parallel to the upper (stationary) solid. Let $u(x,y,t)$ be the separation between the solid walls and assume that the slope $|\nabla u| \ll 1$. We also assume that $u/L \ll 1$, where L is the linear size of the nominal contact region. In this case one expects that the fluid velocity varies slowly with the coordinates x and y as compared to the variation in the orthogonal direction z. Assuming also a slow time dependence, the Navier Stokes equations reduces to

$$\eta\frac{\partial^2\mathbf{v}}{\partial z^2} = \nabla p.$$

Here and in what follows $\mathbf{v} = (v_x, v_y)$, $\mathbf{x} = (x,y)$ and $\nabla = (\partial_x, \partial_y)$ are two-dimensional vectors. Note that $v_z \approx 0$ and that $p(\mathbf{x})$ is independent of z to a good approximation. The solution to the equations above can be written as

$$\mathbf{v} = \frac{1}{2\eta}z(z-u(\mathbf{x}))\nabla p + \left(1-\frac{z}{u(\mathbf{x})}\right)\mathbf{v}_0, \qquad (1)$$

so that $\mathbf{v} = \mathbf{v}_0$ on the solid wall $z = 0$ and $\mathbf{v} = 0$ for $z = u(\mathbf{x})$. Integrating over z (from $z = 0$ to $z = u(\mathbf{x})$) gives the fluid flow vector

$$\mathbf{J} = -\frac{u^3(\mathbf{x})}{12\eta}\nabla p + \frac{1}{2}u(\mathbf{x})\mathbf{v}_0. \qquad (2)$$

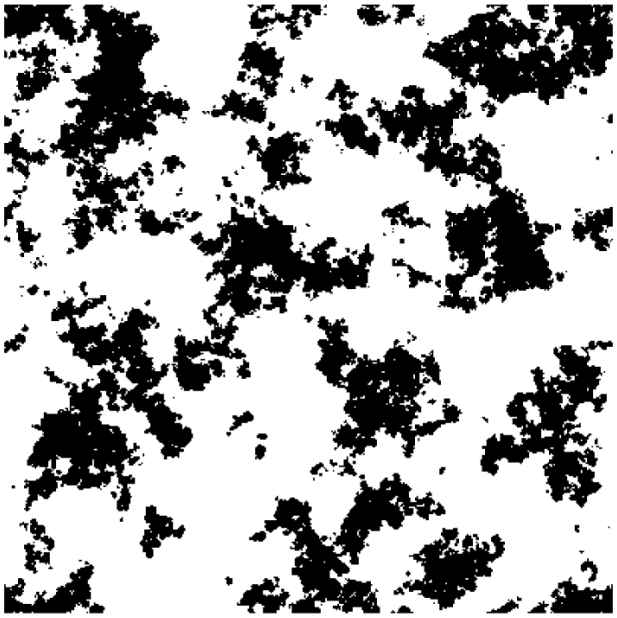

Fig. 2. The black area is the contact between two elastic solids with randomly rough surfaces as obtained using molecular dynamics. For surfaces which have fractal-like roughness the whole way down to the atomic length scale, the contact at the highest magnification (atomic resolution) typically consists of nanometer-sized atomic clusters. Adapted from ref. [17].

Mass conservation demands that

$$\frac{\partial u(\mathbf{x},t)}{\partial t} + \nabla \cdot \mathbf{J} = 0, \tag{3}$$

where the interfacial separation $u(\mathbf{x},t)$ is the volume of fluid per unit area. In this last equation we have allowed for a slow time dependence of $u(\mathbf{x},t)$ as would be the case, *e.g.*, during fluid squeeze-out from the interfacial region between two solids. If an elastic body with a rough surface is sliding at a constant velocity on a rigid flat surface in a fluid, then $u(\mathbf{x},t)$ will (in the reference frame of the moving body) be time independent, and the time derivative in (3) will vanish. However, if both bodies have surface roughness $u(\mathbf{x},t)$ may vary rapidly with time. However, the ensemble average of $u(\mathbf{x},t)$, which is the quantity which enters in the effective equations below, may still be time independent. In this case the effective (or homogenized) mass conservation equation reads $\nabla \cdot \bar{\mathbf{J}} = 0$, where $\bar{\mathbf{J}} = \langle \mathbf{J} \rangle$ denote ensemble averaging.

3 Roughness on many length scales: effective equations of fluid flow and fluid flow factors

The fluid flow at the interface between contacting solids is a very complex problem, in particular at high squeezing pressures where a network of flow channels with rapidly varying width and height may prevail at the interface. This is illustrated in fig. 2 which shows the contact area (black) between two elastic solids with randomly rough surfaces. At pressure higher than that used in the figure, the contact area (black) may percolate which will have a drastic influence on the interfacial fluid flow properties.

Equations (2) and (3) describe the fluid flow at the interface between contacting solids with rough surfaces. One way to integrate out the surface roughness is by using the Renormalization Group (RG) procedure. In this procedure one eliminates or integrates out the surface roughness components in steps and obtains a set of RG flow equations describing how the effective fluid equation evolves as more and more of the surface roughness components are eliminated. One can show that after eliminating all the surface roughness components, the fluid current (given by (2)) takes the form

$$\bar{\mathbf{J}} = A(\bar{u})\nabla\bar{p} + B(\bar{u})\mathbf{v}_0, \tag{4}$$

where A and B are 2×2 matrices, and where $\bar{u}(\mathbf{x},t)$ and $\bar{p}(\mathbf{x},t)$ now are *locally averaged* quantities. In general, A and B depend also on $\nabla\bar{p}$ (see ref. [15] and below).

Equation (4) is usually written as

$$\bar{\mathbf{J}} = -\frac{\bar{u}^3\phi_{\rm p}(\bar{u})}{12\eta_0}\nabla\bar{p} + \frac{1}{2}\bar{u}\mathbf{v}_0 + \frac{1}{2}h_{\rm rms}\phi_{\rm s}(\bar{u})\mathbf{v}_0, \tag{5}$$

where the pressure flow factor $\phi_{\rm p}$ and the shear flow factor $\phi_{\rm s}$ in general (for anisotropic surface roughness) are 2×2 matrices.

Let us define the 2×2 matrix (we use polar coordinates so that the wave vector $\mathbf{q} = q(\cos\phi, \sin\phi)$) [14]

$$D(q) = \frac{\int {\rm d}\phi\, C(\mathbf{q})\mathbf{q}\mathbf{q}/q^2}{\int {\rm d}\phi\, C(\mathbf{q})}, \tag{6}$$

with the surface roughness power spectrum [18]

$$C(\mathbf{q}) = \frac{1}{(2\pi)^2}\int {\rm d}^2x\, \langle h(\mathbf{x})h(\mathbf{0})\rangle {\rm e}^{-i\mathbf{q}\cdot\mathbf{x}}, \tag{7}$$

where $\langle \ldots \rangle$ stands for ensemble average, and where $h(\mathbf{x})$ is the height profile. For roughness with isotropic statistical properties, $C(\mathbf{q})$ will only depend on $q = |\mathbf{q}|$ and in this case $D(q)$ will be diagonal with $D_{11} = D_{22} = 1/2$.

We will assume most of the time that $D(q)$ is independent of q and in this case (6) is equivalent to

$$D = \frac{\int {\rm d}^2q\, C(\mathbf{q})\mathbf{q}\mathbf{q}/q^2}{\int {\rm d}^2q\, C(\mathbf{q})}\,. \tag{8}$$

In this case, in the coordinate system where D is diagonal the matrices $\phi_{\rm p}$ and $\phi_{\rm s}$ will be diagonal too. Note that ${\rm Tr}\, D = D_{11}+D_{22} = 1$, and in the coordinate system where D is diagonal we can write $D_{11} = 1/(1+\gamma)$ and $D_{22} = \gamma/(1+\gamma)$, where $\gamma = \xi_x/\xi_y$ is the Peklenik number. Note that $D_{11}(1/\gamma) = D_{22}(\gamma)$. If $D(q)$ (see (6)) depends on q, we may still define (in the coordinate system where $D(q)$ is diagonal) $\gamma = -1+1/D_{11}$ as before, but the xy-coordinate system where $D(q)$ is diagonal may depend on q (in which case the rotation angle, $\psi(q)$, of the x-axis relative to some fix axis, is important information too; see ref. [14]). In this case γ will depend on q and we will refer to $\gamma(q)$ as the

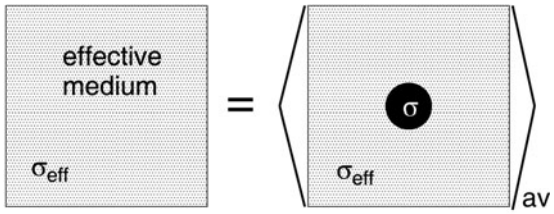

Fig. 3. Effective medium theories take into account random disorder in a physical system, *e.g.*, random fluctuations in the interfacial separation $u(\mathbf{x})$. Thus, for a n-component system (*e.g.*, where the separation u takes n different discrete values) the flow in the effective medium should be the same as the average fluid flow obtained when circular regions of the n-components are embedded in the effective medium. Thus, for example, the pressure p at the origin calculated assuming that the effective medium occurs everywhere must equal the average $\sum c_i p_i$ (where c_i is the concentration of component i) of the pressures p_i (at the origin) calculated with the circular inclusion of component $i = 1, \ldots, n$.

Peklenik function (and $\psi(q)$ as the Peklenik angle). Note that since $D(q)$ is a symmetric tensor and since $\mathrm{Tr}\, D = 1$ the D-matrix has only two independent components. Thus it is fully defined by the Peklenik function $\gamma(q)$ and the Peklenik angle $\psi(q)$.

For large separation between the surfaces compared to the surface roughness amplitude, the surface roughness must have a negligible influence on the fluid flow. This implies that $\phi_\mathrm{p} \to 1$ and $\phi_\mathrm{s} \to 0$ as $\bar{u}/h_\mathrm{rms} \to \infty$. Hence, the effective Reynolds equation reduces to the classical Reynolds equation for smooth surfaces as the film thickness becomes large relative to the rms roughness.

We now show how one may derive approximate expressions for ϕ_p and ϕ_s to be included in eq. (5).

4 Fluid pressure flow factor ϕ_p

Fluid flow at the interface between contacting solids is a very complex process due to the many interconnected flow channels at the interface (see fig. 2). We have used the 2D Bruggeman effective medium theory [19–22] to calculate (approximately) the pressure flow factor. This treatment takes into account the network of flow channels. The basic physics behind the effective medium theory is illustrated in fig. 3. For a two-component system, one assumes that the flow in the effective medium should be the same as the average fluid flow obtained when circular regions of the two components are embedded in the effective medium. Thus, for example, the pressure p at the origin calculated assuming that the effective medium occurs everywhere must equal the average $c_1 p_1 + c_2 p_2$ of the pressures p_1 and p_2 calculated with the circular inclusion of the two components **1** and **2**, respectively.

Using the 2D Bruggeman effective medium theory we get $\phi_\mathrm{p} = 12\eta_0\sigma_\mathrm{eff}/\bar{u}^3$ where, for an anisotropic system, the effective medium flow conductivity σ_eff is a 2×2 matrix. Introduce a xy coordinate system and choose the x-axis along the principal axis of the D-matrix. In this case we can consider σ_eff as a scalar which satisfies

$$\frac{1}{\sigma_\mathrm{eff}} = \int \mathrm{d}u\, P(u) \frac{1+\gamma}{\gamma\sigma_\mathrm{eff} + \sigma(u)}, \tag{9}$$

where $P(u)$ is the probability distribution of interfacial separations, and where

$$\sigma(u) = \frac{u^3}{12\eta_0}\,. \tag{10}$$

Fluid flow along the y-axis is given by a similar equation with γ replaced with $1/\gamma$. The probability distribution $P(u)$ of interfacial separations has been derived in ref. [23] (see also sect. 9). Here we note that $P(u)$ has a delta function at the origin $u = 0$ with the weight determined by the area of real contact

$$P(u) = \frac{A}{A_0}\delta(u) + P_\mathrm{c}(u), \tag{11}$$

where $P_\mathrm{c}(u)$ is a continuous (finite) function of u. Substituting this in (9) gives

$$\frac{1}{\sigma_\mathrm{eff}} = \frac{A}{A_0}\frac{1+\gamma}{\gamma\sigma_\mathrm{eff}} + \int \mathrm{d}u\, P_\mathrm{c}(u) \frac{1+\gamma}{\gamma\sigma_\mathrm{eff} + \sigma(u)}\,. \tag{12}$$

This equation is easy to solve by iteration.

In fig. 4(a) we show the the pressure flow factors ϕ_p as a function of the average interfacial separation $\bar{u}$, for anisotropic surfaces with the Peklenik numbers $\gamma = 1/3$, 1 and 3. Note that $\phi_\mathrm{p} = 0$ for $\bar{u} < \bar{u}_\mathrm{c}$, where $\bar{u}_\mathrm{c}$ is the average interfacial separation where the area of real contact percolates in the direction orthogonal to the fluid flow. In the Bruggeman effective medium theory this occurs when the area of real contact equals $A/A_0 = \gamma/(\gamma+1)$. Thus for $\gamma = 1/3$, 1 and 3 the contact area percolates, *i.e.* no fluid flow occurs along the considered direction, when $A/A_0 = 1/4$, $1/2$ and $3/4$, respectively. This explains why ϕ_p vanishes at much larger (average) interfacial separation (and hence smaller contact area) for $\gamma = 1/3$ as compared to $\gamma = 3$.

In obtaining the results in fig. 4(a) we have used the Persson contact mechanics theory for the contact area A and the probability distribution $P(u)$ (see sect. 9). This theory depends on the elastic energy U_el stored in the asperity contact regions and in this paper we use the simplest version for U_el (see ref. [14]), where the γ-parameter (not the Peklenik number) $= 1$. Comparison of the theory predictions with numerical simulations for small systems has shown that $\gamma \approx 0.45$ gives the best agreement between theory and the (numerical) experiments. However, using $\gamma = 0.45$ (or $\gamma \neq 1$ in general) results in much longer computational time, with relative small numerical changes as compared to using $\gamma = 1$.

5 Fluid shear flow factor ϕ_s

Assume that the normal pressure is so high that the area of real contact percolate. In this case $\phi_\mathrm{p} = 0$ and the

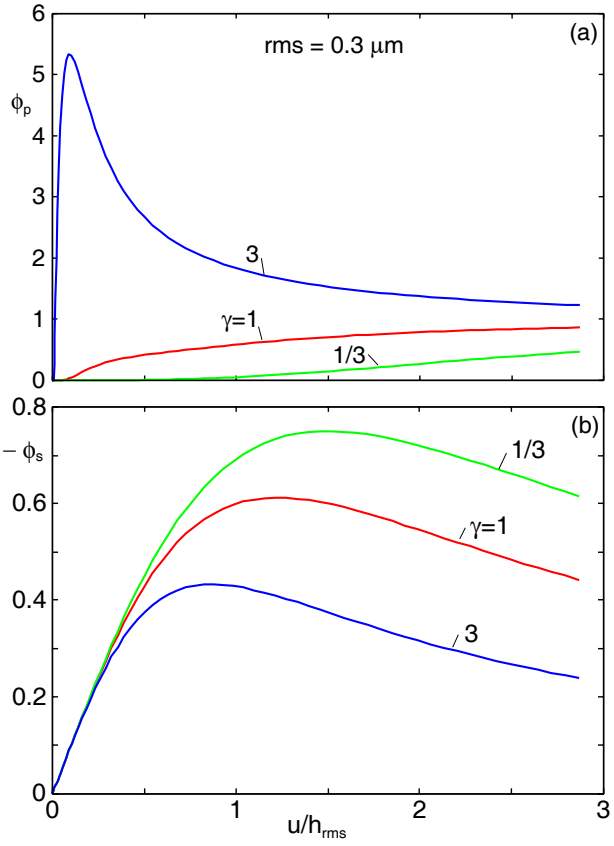

Fig. 4. The pressure and shear flow factors ϕ_p and ϕ_s, as a function of the average interfacial separation $\bar{u}$, for anisotropic surfaces with the Peklenik numbers $\gamma = 1/3$, 1 and 3. In all cases the angular average power spectrum is of the type shown in fig. 9 with $H = 1$ and $h_{rms} = 0.3\,\mu$m.

fluid at the interface is trapped in the roughness cavities of the upper (stationary) solid so that the fluid current $\mathbf{J} = 0$. Thus we conclude that when $\bar{u} < u_c$, where u_c is the average separation between the surfaces when the area of real contact first percolate, then $\phi_s(\bar{u}) = -\bar{u}/h_{rms}$. On the other hand for $\langle h^2\rangle/\bar{u}^2 \ll 1$ we have

$$\phi_s = -\frac{3h_{rms}}{\bar{u}}D.$$

Using $D = 1/(1+\gamma)$ this gives

$$\phi_s = -\frac{3}{1+\gamma}\frac{h_{rms}}{\bar{u}}\,.$$

Again, the flow factor along the y-axis is given by a similar equation with γ replaced with $1/\gamma$. We can interpolate between the two limiting behavior using

$$\phi_s = -\bar{u}/h_{rms}, \qquad (13a)$$

for $\bar{u} < \bar{u}_c$ and

$$\phi_s = -\left(\frac{h_{rms}}{\bar{u}} + \frac{(1+\gamma)}{3}\frac{(\bar{u}-\bar{u}_c)}{h_{rms}}\right)^{-1}, \qquad (13b)$$

for $\bar{u} > \bar{u}_c$. This function is continuous for $u = u_c$ as expected.

In fig. 4(b) we show the shear flow factor ϕ_s as a function of the average interfacial separation $\bar{u}$. Note that for very large $\bar{u}$ we have $\phi_p = 1$ and $\phi_s = 0$. We will refer to these as trivial fluid flow factors. Note also that $\phi_s < 0$, so that this flow term reduces the fluid flow. This is due to the stagnant fluid in the valleys of the stationary rough surface (upper surface in fig. 1).

6 Frictional shear stress factors ϕ_f, ϕ_{fs} and ϕ_{fp}

The shear stress induced by the fluid is

$$\sigma_{fluid} = -\eta_0\frac{\partial v_x}{\partial z} = \frac{\eta_0 v_0}{u(\mathbf{x})} - \frac{1}{2}[2z - u(\mathbf{x})]\nabla p, \qquad (14)$$

where $z = 0$ on the lower surface and $z = u(\mathbf{x})$ on the upper surface. The total shear stress is

$$\sigma = (1 - a(\mathbf{x}))\sigma_{fluid} + a(\mathbf{x})\sigma_f, \qquad (15)$$

where the last term is the contribution from the area of real contact and where $a(\mathbf{x})$ is 1 at dry contact, and 0 elsewhere. Moreover $a = \langle a(\mathbf{x})\rangle = A/A_0$ is the (normalized) contact area calculated with the contact pressure $p_{cont}(\mathbf{x})$, as given, *e.g.*, by the Persson's contact mechanics theory. Using (14) and (15) gives the total frictional (tangential) stress on the bottom solid

$$\langle\sigma\rangle = \bar{\sigma} = \eta_0 v_0\left\langle\frac{1}{u}\right\rangle + \frac{1}{2}\langle u\nabla p\rangle + a\sigma_f, \qquad (16)$$

where

$$\left\langle\frac{1}{u}\right\rangle = \int_{u^*}^{\infty} \mathrm{d}u\, P(u)\frac{1}{u}\,. \qquad (17)$$

As before, $P(u)$ is the probability distribution of interfacial separations. Note that $P(u)$ depends on the local (average) contact pressure $p_{cont}(\mathbf{x})$. In (17) we have introduced a cut-off distance $u^* > 0$ of order a few nanometer. This takes into account that the fluid cannot be described using continuum mechanics when the separation is of order a few nanometers. In addition, the relation between the shear stress and the shear rate for nanometer thick confined (fluid) films will not be linear (as for a Newtonian fluid), but will behave more like a soft solid. The total frictional stress acting on the upper solid is also given by (16). This can be seen as follows. The shear stress from the fluid acting on the upper solid is given by (14) with $z = u(\mathbf{x})$

$$\sigma_{fluid} = \frac{\eta_0 v_0}{u(\mathbf{x})} - \frac{1}{2}u(\mathbf{x})\nabla p. \qquad (18)$$

However, there will be an additional frictional stress acting on the upper solid induced by the pressure p and given by

$$-p\nabla u = -\nabla(pu) + u\nabla p,$$

where $-\nabla u$ is the tangential component of the unit vector orthogonal to the surface $z = u(\mathbf{x})$ at point $\mathbf{x}$ (we assume $|\nabla u| \ll 1$). We are interested in the friction force and can neglect contribution $-\nabla(pu)$ because the integral over the total surface this term vanish. Adding the term $u\nabla p$ to (18) gives the expression (16) for the total frictional stress acting on the upper solid.

When the contact area percolates (for $\bar{u} < \bar{u}_c$), the fluid trapped in the cavities must satisfy $\mathbf{J} = \mathbf{0}$ or

$$\mathbf{J} = -\frac{u^3(\mathbf{x})}{12\eta_0}\nabla p + \frac{1}{2}u(\mathbf{x})\mathbf{v}_0 = \mathbf{0}.$$

Thus for $\bar{u} < \bar{u}_c$

$$u\nabla p = 6\eta_0 \mathbf{v}_0 \frac{1}{u}$$

and

$$\langle u\nabla p\rangle = 6\eta_0\mathbf{v}_0\left\langle\frac{1}{u}\right\rangle. \tag{19}$$

On the other hand for $\bar{u} \gg h_{\rm rms}$ we have, using (A.9),

$$\begin{aligned}\langle u\nabla p\rangle &= \bar{u}\nabla\bar{p} + \langle u_1\nabla p_1\rangle \\ &= \bar{u}\nabla\bar{p} + \int \mathrm{d}^2q\, C(\mathbf{q})\frac{\mathbf{qq}}{q^2}\cdot\left(\frac{6\eta_0}{\bar{u}^3}\mathbf{v}_0 - \frac{3}{\bar{u}}\nabla\bar{p}\right) \\ &= \bar{u}\nabla\bar{p} + \langle h^2\rangle D\left(\frac{6\eta_0}{\bar{u}^3}\mathbf{v}_0 - \frac{3}{\bar{u}}\nabla\bar{p}\right).\end{aligned}$$

This expression is valid to first order in $\langle h^2\rangle/\bar{u}^2$ and to this order it can be approximated as (neglecting the fluid induced asperities flattening)

$$\langle u\nabla p\rangle = \frac{\bar{u}^3}{\bar{u}^2 + 3\langle h^2\rangle D}\nabla\bar{p} + \frac{6\eta_0}{\bar{u}^3}\langle h^2\rangle D\mathbf{v}_0. \tag{20}$$

We can smoothly interpolate between the result (19) for $\bar{u} < \bar{u}_c$ and (20) valid for $\bar{u} \gg h_{\rm rms}$ using

$$\begin{aligned}\langle u\nabla p\rangle = &\frac{\bar{u}^2(\bar{u}-\bar{u}_c)\theta(\bar{u}-\bar{u}_c)}{\bar{u}^2 + 3\langle h^2\rangle D}\nabla\bar{p} \\ &+ \frac{6\eta_0}{\langle u^{-1}\rangle^{-1} + \theta(\bar{u}-\bar{u}_c)(\bar{u}-\bar{u}_c)(\bar{u}^2/\langle h^2\rangle)D^{-1}}\mathbf{v}_0,\end{aligned} \tag{21}$$

where $\theta(x) = 1$ for $x > 0$ and zero otherwise. This expression is exact for $\bar{u} < \bar{u}_c$ and exhibits the asymptotically correct behavior for $\bar{u} \gg h_{\rm rms}$. In addition it is continuous at $\bar{u} = \bar{u}_c$.

Following Patir and Cheng, we write the average shear stress as

$$\bar{\sigma} = (\phi_f + \phi_{fs})\frac{\eta_0\mathbf{v}_0}{\bar{u}} + \phi_{fp}\frac{1}{2}\bar{u}\nabla\bar{p} + \frac{A}{A_0}\sigma_f, \tag{22}$$

where

$$\phi_f = \bar{u}\left\langle\frac{1}{u}\right\rangle, \tag{23}$$

$$\phi_{fs} = \frac{3\bar{u}}{\langle u^{-1}\rangle^{-1} + \theta(\bar{u}-\bar{u}_c)(\bar{u}-\bar{u}_c)(\bar{u}^2/\langle h^2\rangle)D^{-1}}, \tag{24}$$

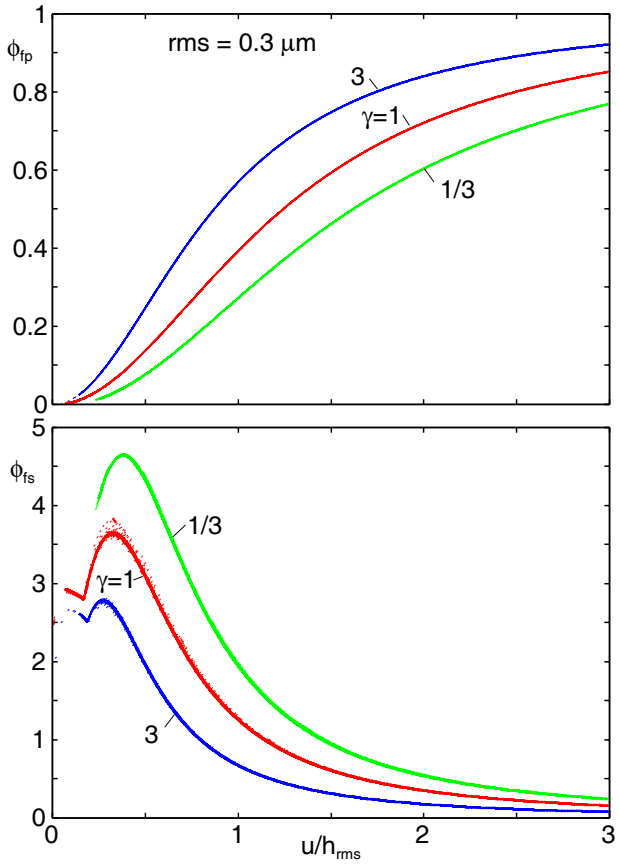

Fig. 5. The friction pressure and shear stress factors ϕ_{fp} and ϕ_{fs}, as a function of the average interfacial separation $\bar{u}$, for anisotropic surfaces with the Peklenik numbers $\gamma = 1/3$, 1 and 3. In all cases the angular average power spectrum is of the type shown in fig. 9 with $H = 1$ and $h_{\rm rms} = 0.3\,\mu$m.

and

$$\phi_{fp} = \frac{\bar{u}(\bar{u}-\bar{u}_c)\theta(\bar{u}-\bar{u}_c)}{\bar{u}^2 + 3\langle h^2\rangle D}. \tag{25}$$

In fig. 5 we show the friction pressure and shear stress factors ϕ_{fp} and ϕ_{fs}, as a function of the average interfacial separation $\bar{u}$, for anisotropic surfaces with the Peklenik numbers $\gamma = 1/3$, 1 and 3. Note that, as expected, for very large $\bar{u}$ we have $\phi_f = \phi_{fp} = 1$ and $\phi_{fs} = 0$. We will refer to these as trivial friction factors. Note also that the ϕ_{fs} contribution to the shear stress is positive. The physical origin of this contribution can be understood as follows: The fluid in the valleys of the stationary rough surface (see fig. 1) will be mostly stagnant and hence the effective fluid film thickness (which undergoes shear) in the valley regions will be thinner (say $\tilde{u}$) than given by the local film thickness u. This will result in a higher frictional shear stress $\eta\mathbf{v}_0/\tilde{u}$ than expected if $\tilde{u}$ were the local interfacial separation $\bar{u}$.

7 Viscosity of confined fluids: shear thinning

It is well known that the viscosity of fluids at high pressures may be many orders of magnitude larger than at

low pressures. Using the theory of activated processes, and assuming that a local molecular rearrangement in a fluid results in a local volume expansion, one expects an exponential dependence on the hydrostatic pressure $\eta = \eta_0 \exp(p/p_0)$, where typically (for hydrocarbons or polymer fluids) $p_0 \approx 10^8$ Pa (see, *e.g.*, refs. [24, 25]). Here we are interested in (wetting) fluids confined between the surfaces of elastically soft solids, *e.g.*, rubber or gelatin. In this case the pressure at the interface is usually at most of order of the Young's modulus, which (for rubber) is less than 10^7 Pa. Thus, in most cases involving elastically soft materials, the viscosity can be considered as independent of the local pressure.

It has been observed experimentally [26, 27], and also found in Molecular Dynamics (MD) simulations [28, 29], that the effective viscosity η (defined by $\sigma = \eta v/u$, where σ is the shear stress, u the separation between the surfaces and v the relative velocity) of very thin (nanometer thickness) fluid films confined between solid walls at low pressure may exhibit non-Newtonian properties. In addition, for nanometer wall-wall separations, a finite normal stress is necessary for the squeeze-out, *i.e.*, the "fluid" now behaves as a soft solid and the squeeze-out occurs in a quantized way by removing one monolayer after another with increasing normal stress [30]. In the present study we will consider the solid-like monolayers which may be attached to the solid walls as part of the solids and characterized with a shear stress $\sigma_{\rm f}$. The latter can be considered as independent of the local normal stress at the low stresses which prevail when at least one of the solids is made from a rubber-like material.

Many fluids, in particular polymer fluids, *e.g.*, high viscosity silicon oil, undergoes shear thinning at relative low shear rate. The viscosity is often well approximated by

$$\eta(u, v) = \frac{\eta_0}{1 + (\eta_0/B)\dot\gamma^n}\,, \tag{26}$$

(or similar empirical relations, see *e.g.* ref. [31]) where the shear rate $\dot\gamma = v/u$ and where the exponent n is typically $n \approx 0.9$ [26]. If η_0 is in units of Pa s and $\dot\gamma$ in units of $\rm s^{-1}$, then $B \approx 8.0 \times 10^4$. In this model shear thinning start when $\dot\gamma \approx \dot\gamma_{\rm c} = (B/\eta_0)^{1/n}$. For example, for silicon oil with the low shear rate viscosity $\eta_0 = 10$ Pa s the critical shear rate $\dot\gamma_{\rm c} \approx 10^4\,{\rm s}^{-1}$. In the theory above we can take into account the dependence of η on the interfacial separation u (and the sliding velocity v) by simply replacing η_0 in (5) with η given by (26). Note that this is equivalent to a modification of the pressure flow factor and will, from a numerically point of view, not lead to a more complex problem than without the shear thinning. It is also necessary to include the shear thinning when calculating the frictional shear stress. Thus in (22)–(24) we replace the term $\langle u^{-1}\rangle$ with

$$\left\langle \frac{\eta(u,v)}{\eta_0 u} \right\rangle = \int_{u^*}^{\infty} {\rm d}u\, P(u) \frac{\eta(u,v)}{\eta_0 u}\,, \tag{27}$$

while in the velocity factor $\eta_0 \mathbf{v}/\bar u$ in (22) remains unchanged. Observe that the probability distribution of interfacial separations, $P(u)$, depends on $p_{\rm cont}(\mathbf{x})$. We show below that shear thinning will strongly reduce the divergence of u^{-1} as $u \to 0$, and make the result less sensitive to the exact value of the cut-off u^*.

8 Elastic asperity deformation by the fluid pressure

The surface roughness profile will deform not just because of the direct contact between the solids, but also because of the rapidly fluctuating fluid pressure distribution which prevails at the asperity length scale. This effect was neglected in the analysis presented above and in most earlier studies of this subject. We have recently studied the influence of the fluid pressure on the roughness profile and shown that the fluid pressure effectively reduces the roughness amplitude and introduce surface roughness anisotropy which we refer to as dynamically induced anisotropy [15].

The power spectrum of the deformed surface profile can be written (approximately) as

$$\tilde C(\mathbf{q}) = \frac{C(\mathbf{q})}{|S(\mathbf{q})|^2}\,, \tag{28}$$

where

$$S(\mathbf{q}) = 1 + \frac{6}{E^* \bar u q^3}(i\mathbf{q}) \cdot \left[\nabla \bar p - \frac{2\eta}{\bar u^2}\mathbf{v}_0\right]. \tag{29}$$

Note that $|S(\mathbf{q})| > 1$, so that the fluid pressure distribution effectively smooths the surface profile. Note also that even if the surface roughness is isotropic, the effective surface profile during sliding will be anisotropic. In the study below we will not include the deformation of the surface roughness profile by the fluid pressure, but we will calculate $\tilde C(\mathbf{q})$ from the interfacial and pressure distributions obtained without accounting for the effects of fluid deformations on the surface roughness profile (non-self-consistent procedure).

9 Elastohydrodynamics for cylinder

Consider the stationary sliding of a cylinder on a flat rough substrate. The ensemble-averaged fluid flow vector $\bar{\mathbf{J}}$ satisfies $\nabla \cdot \bar{\mathbf{J}} = 0$ or ${\rm d}\bar J_x/{\rm d}x = 0$. Thus $\bar J_x = v_0 u^*/2$ where u^* is a constant. Using the x-component of (5) gives

$$-\frac{\bar u^3 \phi_p(\bar u)}{12\eta_0}\frac{{\rm d}\bar p}{{\rm d}x} + \frac{1}{2}\bar u v_0 + \frac{1}{2}h_{\rm rms}\phi_s(\bar u)v_0 = \frac{1}{2}v_0 u^*, \tag{30}$$

or

$$\frac{{\rm d}\bar p}{{\rm d}x} = \frac{6\eta_0 v_0}{\bar u^3 \phi_p(\bar u)}\left(\bar u + h_{\rm rms}\phi_s(\bar u) - u^*\right), \tag{31}$$

where ϕ_s and ϕ_p have been determined in sects. 4 and 5. Hereinafter we will denote the (locally averaged) fluid pressure $\bar p$ as $p_{\rm fluid}(\mathbf{x}, t)$. When solving for the fluid flow between macroscopic surfaces with roughness, in a mean-field type of treatment one writes the local nominal pressure (*i.e.*, the pressure locally averaged over surface area

with linear dimension of order the wavelength λ_0 of the longest surface roughness component) as [32]

$$p(\mathbf{x},t) = p_{\rm fluid}(\mathbf{x},t) + p_{\rm solid}(\mathbf{x},t), \tag{32}$$

where $p_{\rm fluid}$ and $p_{\rm solid}$ are locally averaged nominal fluid pressure and solid wall-wall contact pressure, respectively. The fluid pressure satisfies (31), while the contact pressure $p_{\rm solid}$ can be related to the interfacial separation $\bar{u}(\mathbf{x},t)$ using the contact mechanics theory of Persson (see refs. [7,8]). In particular, for large enough average surface separation it can be shown that [7]

$$p_{\rm solid} \approx \beta E^* e^{-\bar{u}/u_0},$$

where β and u_0 can be calculated from the surface roughness power spectrum. Here we will briefly review the contact mechanics model of Persson which we use in this study.

Consider the frictionless contact between two elastic solids with the Young's elastic modulus E_0 and E_1 and the Poisson ratios ν_0 and ν_1. Assume that the solid surfaces have the height profiles $h_0(\mathbf{x})$ and $h_1(\mathbf{x})$, respectively. The elastic contact mechanics for the solids is equivalent to those of a rigid substrate with the height profile $h(\mathbf{x}) = h_0(\mathbf{x}) + h_1(\mathbf{x})$ and a second elastic solid with a flat surface and with the Young's modulus E and the Poisson ratio ν chosen so that [33]

$$\frac{1-\nu^2}{E} = \frac{1-\nu_0^2}{E_0} + \frac{1-\nu_1^2}{E_1}. \tag{33}$$

The contact mechanics formalism developed elsewhere [7,8,34,35] is based on studying the interface between two contacting solids at different magnification ζ. When the system is studied at the magnification ζ it appears as if the contact area (projected on the xy-plane) equals $A(\zeta)$, but when the magnification increases it is observed that the contact is incomplete (see fig. 6), and the surfaces in the apparent contact area $A(\zeta)$ are in fact separated by the average distance $\bar{u}(\zeta)$, see fig. 7. The (apparent) relative contact area $A(\zeta)/A_0$ at the magnification ζ is given by [8,34]

$$\frac{A(\zeta)}{A_0} = \frac{1}{(\pi G)^{1/2}} \int_0^{p_0} {\rm d}\sigma\, {\rm e}^{-\sigma^2/4G} = {\rm erf}\left(\frac{p_0}{2G^{1/2}}\right), \tag{34}$$

where

$$G(\zeta) = \frac{\pi}{4}\left(\frac{E}{1-\nu^2}\right)^2 \int_{q_0}^{\zeta q_0} {\rm d}q q^3 C(q) \tag{35}$$

and where the surface roughness power spectrum

$$C(q) = \frac{1}{(2\pi)^2} \int {\rm d}^2x \langle h(\mathbf{x}) h(\mathbf{0})\rangle {\rm e}^{-i\mathbf{q}\cdot\mathbf{x}}.$$

Here $\langle \ldots \rangle$ stands for an ensemble average and $p_0 = p_{\rm solid}(\mathbf{x},t)$. The height profile $h(\mathbf{x})$ of the rough surface can be measured routinely today on all relevant length scales using optical and stylus experiments.

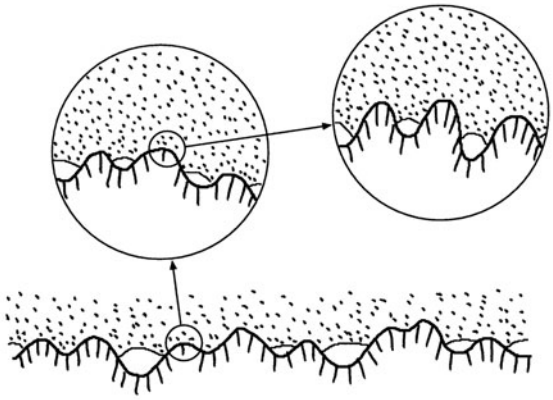

Fig. 6. A rubber block (dotted area) in adhesive contact with a hard rough substrate (dashed area). The substrate has roughness on many different length scales and the rubber makes partial contact with the substrate on all length scales. When a contact area is studied at low magnification it appears as if complete contact occur, but when the magnification is increased it is observed that in reality only partial contact occurs.

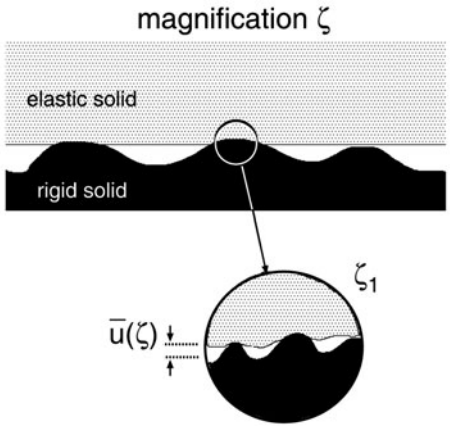

Fig. 7. An asperity contact region observed at magnification ζ. It appears that complete contact occurs in the asperity contact region, but when the magnification is increasing to the highest (atomic scale) magnification ζ_1, it is observed that the solids are actually separated by the average distance $\bar{u}(\zeta)$.

The quantity $\bar{u}(\zeta)$, defined as the average separation between the surfaces in the apparent contact regions observed at the magnification ζ (see fig. 7), can be calculated from [8]

$$\bar{u}(\zeta) = \sqrt{\pi} \int_{\zeta q_0}^{q_1} {\rm d}q\, q^2 C(q) w(q,\zeta) \times \int_{p(\zeta)}^{\infty} {\rm d}p' \frac{1}{p'} e^{-[w(q,\zeta)p'/E^*]^2}, \tag{36}$$

where $p(\zeta) = p_0 A_0/A(\zeta)$ and

$$w(q,\zeta) = \left(\pi \int_{\zeta q_0}^{q} {\rm d}q'\, q'^3 C(q')\right)^{-1/2}.$$

We define $u_1(\zeta)$ to be the (average) height separating the surfaces which appear to come into contact when the

magnification decreases from ζ to $\zeta - \Delta\zeta$, where $\Delta\zeta$ is a small (infinitesimal) change in the magnification. $u_1(\zeta)$ is a monotonically decreasing function of ζ, and can be calculated from the average interfacial separation $\bar{u}(\zeta)$ and $A(\zeta)$ using (see ref. [8])

$$u_1(\zeta) = \bar{u}(\zeta) + \bar{u}'(\zeta)A(\zeta)/A'(\zeta). \tag{37}$$

One can show [22] from the equations above that, as the applied squeezing pressure $p_0 \to 0$, for the magnifications most relevant for calculating fluid flow (*e.g.*, the leak rate of seals) $u_1 \to \bar{u}$.

The probability distribution $P(u)$ of interfacial separations u can be written as $P(u) = (A/A_0)\delta(u) + P_{\rm c}(u)$, where [23]

$$P_{\rm c} \approx \frac{1}{A_0}\int {\rm d}\zeta \frac{[-A'(\zeta)]}{(2\pi h^2_{\rm rms}(\zeta))^{1/2}} \times \left[\exp\left(-\frac{(u-u_1(\zeta))^2}{2h^2_{\rm rms}(\zeta)}\right) + \exp\left(-\frac{(u+u_1(\zeta))^2}{2h^2_{\rm rms}(\zeta)}\right)\right]. \tag{38}$$

Here $h^2_{\rm rms}(\zeta)$ is the mean-square roughness including only roughness wavelength components with $q > q_0\zeta$, which can be obtained from the surface roughness power spectrum using

$$h^2_{\rm rms}(\zeta) = \int_{q_0\zeta}^{q_1} {\rm d}^2q\, C(\mathbf{q}).$$

Note that

$$\int_0^\infty {\rm d}u\, P_{\rm c}(u) = \frac{1}{A_0}\int_1^{\zeta_1} {\rm d}\zeta[-A'(\zeta)] = \frac{A(1)-A(\zeta_1)}{A_0}.$$

Since $A(\zeta_1) = A$ is the area of real contact and $A(1) = A_0$ the nominal contact area, the probability normalization condition

$$\int_0^\infty {\rm d}u\, P(u) = \frac{A}{A_0} + \frac{A_0 - A}{A_0} = 1$$

is satisfied. Using (38) we can calculate the effective fluid conductivity (for anisotropic roughness) using

$$\frac{1}{\sigma_{\rm eff}} = \frac{A}{A_0}\frac{1+\gamma(\zeta_1)}{\gamma(\zeta_1)\sigma_{\rm eff}} + \frac{1}{A_0}\int {\rm d}\zeta \frac{[-A'(\zeta)]}{(2\pi h^2_{\rm rms}(\zeta))^{1/2}} \int_0^\infty {\rm d}u \frac{1+\gamma(\zeta)}{\gamma(\zeta)\sigma_{\rm eff} + \sigma(u)} \times \left[\exp\left(-\frac{(u-u_1(\zeta))^2}{2h^2_{\rm rms}(\zeta)}\right) + \exp\left(-\frac{(u+u_1(\zeta))^2}{2h^2_{\rm rms}(\zeta)}\right)\right], \tag{39}$$

where $\sigma(u) = u^3/12\eta$. This equation is very general but assumes that the Peklenik angle ψ is constant. If the Peklenik angle depends on ζ (or $q = q_0\zeta$), the more general theory developed in ref. [14] must be used. However, in many practical applications one expects the Peklenik angle to be nearly constant, *e.g.*, for surfaces polished or grinded in one direction, or for surfaces where the anisotropy is generated dynamically (see sect. 8).

The elastic deformation equation links the average pressure $p(\mathbf{x}, t)$ to the avegare interfacial separation $\bar{u}$ [33]. For a cylinder contact

$$\bar{u}(x) = u_0 + \frac{x^2}{2R} - \frac{2}{\pi E^*}\int_{-\infty}^{\infty} {\rm d}x'\, p(x') \ln\left|\frac{x-x'}{x'}\right|, \tag{40}$$

where u_0 is the average central separation (*i.e.* $u_0 = u(x = 0)$). u_0 can be calculated with the load balance equation

$$\int_{-\infty}^{\infty} {\rm d}x'\, p(x') = F_{\rm N}/L. \tag{41}$$

Equations (30), (32), (36) (for $\zeta = 1$), (40) and (41) represent 5 equations for the 5 unknown variables p, $p_{\rm fluid}$, $p_{\rm solid}$, $\bar{u}$ and u_0. In the theory presented above, cavitation is assumed to occur only on the macroscopic scale.

10 Numerical results

We will present numerical results to illustrate the theory developed above. We focus on the contact between a rubber cylinder (radius R) with surface roughness and a flat hard substrate (*e.g.*, glass) lubricated by a fluid. We will consider two different cases, namely one case with relative low nominal rubber-substrate contact pressure and a second case with very high contact pressure as is typical for many engineering application, *e.g.*, for wiper blades or syringes. Details about the adopted numerical procedure for the resolution of the lubrication problem are reported in appendix B.

The low-pressure system consists of a rubber cylinder with the radius $R = 1\,{\rm cm}$ and an elastic modulus $E = 10\,{\rm MPa}$ with three different (self-affine fractal) surfaces with the root-mean-square roughness $h_{\rm rms} = 0.3$, 1 and $3\,\mu{\rm m}$ and fractal dimension $D_{\rm f} = 2.2$. The power spectra of the $h_{\rm rms} = 0.3\,\mu{\rm m}$ surface is shown in fig. 8 (red line). The load on the cylinder per unit length $F_{\rm N}/L = 100\,{\rm N/m}$, giving a (static) Hertz contact region with the half-width $a_{\rm H} = 0.31\,{\rm mm}$, and the maximum and average Hertz contact pressures $p_{\rm max} = 0.21\,{\rm MPa}$ and $p_{\rm av} = 0.16\,{\rm MPa}$, respectively.

The high pressure system consists of a rubber cylinder with the radius $R = 0.7\,{\rm mm}$ and elastic modulus $E = 3\,{\rm MPa}$ with a (self-affine fractal) surface with root-mean-square roughness $h_{\rm rms} = 0.3\,\mu{\rm m}$ and fractal dimension $D_{\rm f} = 2$. The power spectra of the surface is shown in fig. 8 (blue line). The load on the cylinder per unit length $F_{\rm N}/L = 200\,{\rm N/m}$ giving a (static) Hertz contact region with the half-width $a_{\rm H} = 0.21\,{\rm mm}$, and the maximum and average Hertz contact pressures $p_{\rm max} = 0.60\,{\rm MPa}$ and $p_{\rm av} = 0.47\,{\rm MPa}$, respectively. We also consider a higher load case with $F_{\rm N}/L = 1000\,{\rm N/m}$, where the (static) Hertz contact region has the half-width $a_{\rm H} = 0.47\,{\rm mm}$, and the maximum and average Hertz contact pressure are $p_{\rm max} = 1.35\,{\rm MPa}$ and $p_{\rm av} = 1.06\,{\rm MPa}$, respectively.

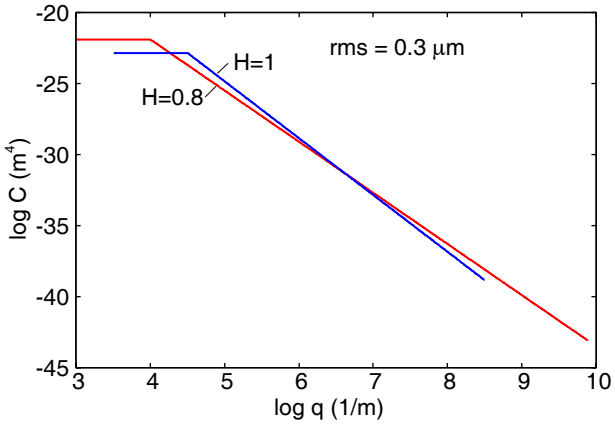

Fig. 8. (Colour on-line) Two surface roughness power spectra used in the calculations. The logarithm (with 10 as basis) of the power spectrum as a function of the logarithm of the wave vector. Red curve: the surface is a self-affine fractal for $q > q_0 = 10^4\,\mathrm{m}^{-1}$ with fractal dimension $D_\mathrm{f} = 2.2$ (Hurst exponent $H = 0.8$). The large wave vector cut off $q_1 = 7.8 \times 10^9\,\mathrm{m}^{-1}$. For $q_L < q < q_0$ the power spectrum is constant with $q_L = 10^3\,\mathrm{m}^{-1}$. Blue curve: $q_0 = 316\,\mathrm{m}^{-1}$ and the fractal dimension $D_\mathrm{f} = 2$ (Hurst exponent $H = 1$). The large wave vector cut off $q_1 = 3.16 \times 10^8\,\mathrm{m}^{-1}$. For $q_L < q < q_0$ the power spectrum is constant with $q_L = 3.16 \times 10^4\,\mathrm{m}^{-1}$. The root-mean-square roughness of both surface is $h_\mathrm{rms} = 0.3\,\mu$m.

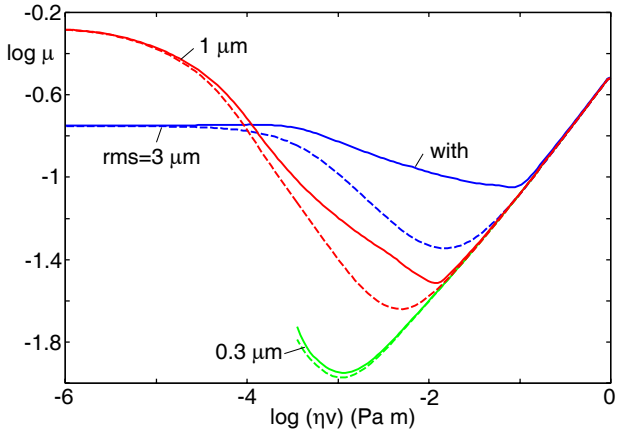

Fig. 9. (Colour on-line) The logarithm (with 10 as basis) of the friction coefficient as a function of the logarithm of the product ηv between the viscosity η and the velocity v. For an elastic cylinder (radius $R = 1\,$cm, elastic modulus $E = 10\,$MPa) sliding on a hard substrate in a fluid with viscosity $\eta = 0.1\,$Pa s. The cylinder has surface roughness with a power spectrum of the type shown in fig. 8 (red curve), with the root-mean-square (rms) roughness $h_\mathrm{rms} = 3$, 1 and $0.3\,\mu$m. The frictional shear stress in the area of real contact $\sigma_\mathrm{f} = 1\,$MPa. The load on the cylinder per unit length $F_\mathrm{N}/L = 100\,$N/m. The static Hertz contact region has half-width $a_\mathrm{H} = 0.31\,$mm and the maximum and average Hertz contact pressure are $p_\mathrm{max} = 0.21\,$MPa and $p_\mathrm{av} = 0.16\,$MPa, respectively. The solid lines include all flow factors while the dashed lines are with trivial frictional shear stress factors ($\phi_\mathrm{f} = \phi_\mathrm{fp} = 1$ and $\phi_\mathrm{fs} = 0$). All cases include shear thinning.

10.1 Low-pressure system

In fig. 9 we show the logarithm (with 10 as basis) of the friction coefficient as a function of the logarithm of the product ηv between the viscosity η and the velocity v. The fluid viscosity $\eta = 0.1\,$Pa s and the rubber cylinder has surface roughness with power spectra of the type shown in fig. 8 (red curve), with the root mean square (rms) roughness $h_\mathrm{rms} = 3$, 1 and $0.3\,\mu$m. The solid lines include all fluid flow and friction shear stress factors, while the dashed lines are with trivial frictional shear stress factors ($\phi_\mathrm{f} = \phi_\mathrm{fp} = 1$ and $\phi_\mathrm{fs} = 0$). In all cases shear thinning is included and the shear stress in the area of real contact is $\sigma_\mathrm{f} = 1\,$MPa. In the hydrodynamic region (high velocity), where $\bar{u} \gg h_\mathrm{rms}$, all the surfaces give the same friction as expected. That is, when the interfacial separation is everywhere much larger than the surface roughness amplitude, then the friction is independent of the surface roughness. Moreover, when the surface roughness amplitude increases the minimum in the friction curves moves to higher velocities [32]. In the boundary lubrication limit (low velocities) the friction increases when the surface roughness decreases. This just reflects the dependence of the area of real contact on the surface roughness amplitude, since we have assumed that the shear stress σ_f is independent of the normal stress.

Note that the difference between the full calculation (solid lines), and the result obtained when using trivial friction shear stress factors (dashed lines), increases as the surface roughness increases. The difference is mainly due to the approximation $\phi_\mathrm{f} = 1$, *i.e.*, the use (in the calculation of the frictional shear stress) of $\langle u \rangle^{-1}$ (dashed lines) in contrast to the correct result $\langle u^{-1} \rangle$ used in the full calculation (solid lines). This approximation is more severe the larger the surface roughness.

In fig. 10 we show the logarithm of the friction coefficient as a function of the logarithm of ηv for the $h_\mathrm{rms} = 3\,\mu$m surface. The solid blue line is the full theory while the dashed blue line is the result with trivial frictional shear stress factors (both curves from fig. 9). The green line is the result with trivial fluid flow and frictional shear stress factors, and all cases include shear thinning. As pointed out above, the large difference between the full calculation and the other cases is mainly due to the difference between using $\bar{u}^{-1} = \langle u \rangle^{-1}$ (the two lower curves) and $\langle u^{-1} \rangle$ (upper curve, full theory).

In fig. 11 we show the same results as in fig. 10 but for the $h_\mathrm{rms} = 1\,\mu$m system in fig. 9. Note that in this case with lower surface roughness the difference between using $\bar{u}^{-1} = \langle u \rangle^{-1}$ (the two lower curves) and $\langle u^{-1} \rangle$ (upper curve, full theory) is much smaller than in the case of larger roughness in fig. 10.

In fig. 12 we show the friction coefficient as a function of the logarithm of ηv for the (a) $h_\mathrm{rms} = 3\,\mu$m and (b) $h_\mathrm{rms} = 1\,\mu$m surfaces. The solid red and blue line represent the full theory while the dashed red and blue lines are the result with trivial frictional shear stress factors (both curves from fig. 9). The green lines represent the full theory without shear thinning. Note that without shear thinning the friction curve exhibits a local maximum

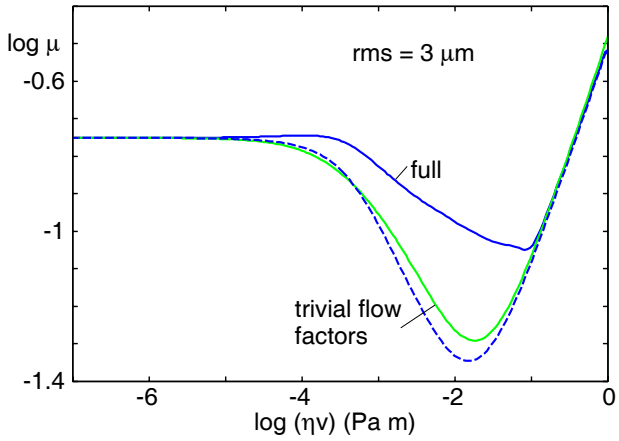

Fig. 10. (Colour on-line) The logarithm (with 10 as basis) of the friction coefficient as a function of the logarithm of the product ηv between the viscosity η and the velocity v for the $h_{\rm rms} = 3\,\mu$m system in fig. 9. The solid blue line is the full theory while the dashed blue line represent the result with trivial frictional shear stress factors (both curves from fig. 9). The green line represent the result with trivial fluid and frictional shear stress factors. All cases include shear thinning (see text for details).

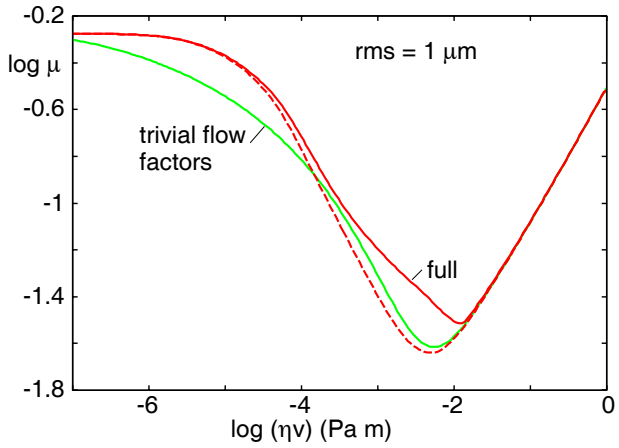

Fig. 11. (Colour on-line) The logarithm (with 10 as basis) of the friction coefficient as a function of the logarithm of the product ηv between the viscosity η and the velocity v for the $h_{\rm rms} = 1\,\mu$m system in fig. 9. The solid blue line is the full theory while the dashed blue line is the result with trivial frictional shear stress factors (both curves from fig. 9). The green line is the result with trivial fluid and frictional shear stress factors. All cases include shear thinning (see text for details).

close to the velocity where the friction curve would exhibit the minimum when shear thinning is included. This effect is due to the influence of shear thinning on the u^{-1} singularity in the term $\langle \eta(u) u^{-1} \rangle$ which occurs in the expression for the frictional shear stress (see (16)). That is, the shear thinning reduces the u^{-1} singularity and hence the contribution to the friction from the term $\langle \eta(u) u^{-1} \rangle$ (see sect. 7). Note that the influence of the shear thinning increases as the surface roughness amplitude $h_{\rm rms}$ increases.

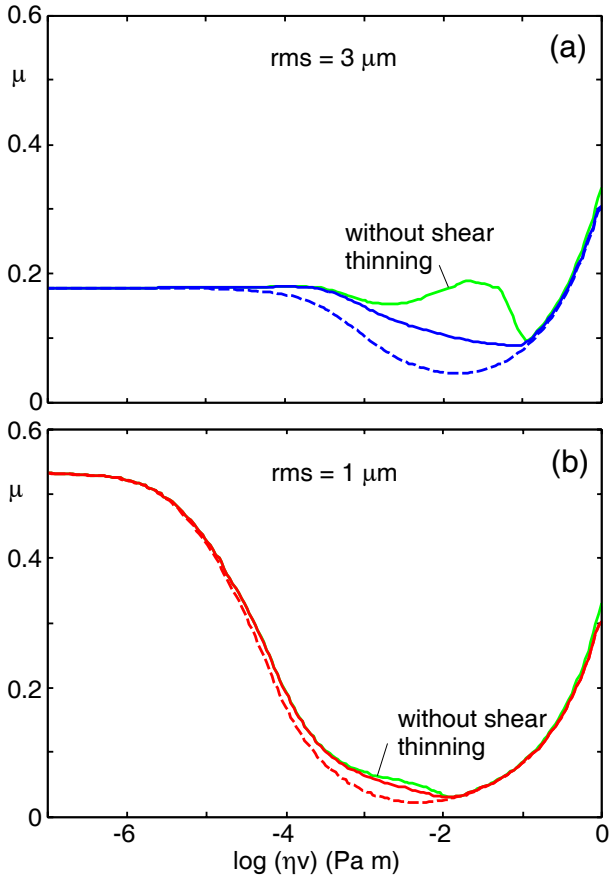

Fig. 12. (Colour on-line) The friction coefficient as a function of the logarithm (with 10 as basis) of the product ηv between the viscosity η and the velocity v for the (a) $h_{\rm rms} = 3\,\mu$m and (b) $h_{\rm rms} = 1\,\mu$m systems in fig. 9. The solid red and blue line represent the full theory while the dashed red and blue line represent the result with trivial frictional shear stress factors (both curves from fig. 9). The green lines represent the full theory without shear thinning.

In fig. 13 we show the same results as in fig. 12 but with a logarithmic scale for the friction coefficient.

All the numerical results presented above are for surfaces with roughness with isotropic statistical properties. In fig. 14 we show the friction coefficient as a function of the logarithm of the product ηv for anisotropic surfaces with the Peklenik numbers $\gamma = 1/3$, 1 and 3. In all cases the angular averaged power spectrum is of the type shown in fig. 9, with $H = 0.8$ and $h_{\rm rms} = 3\,\mu$m. The blue lines represent the full theory with shear thinning, while the green lines represent the full theory without shear thinning.

Figure 15 shows the measured friction coefficient as a function of the product ηv (log-log scale) for the contact between a (hard) spherical ball and a flat rubber surface [36]. Results are shown both for a relative smooth surface ($h_{\rm rms} \approx 0.1\,\mu$m) and for another rubber surface which was crosslinked against a sandblasted and unidirectionally polished or grinded surface with $h_{\rm rms} \approx 10\,\mu$m. The lubricant fluid in the study (mixtures of glyc-

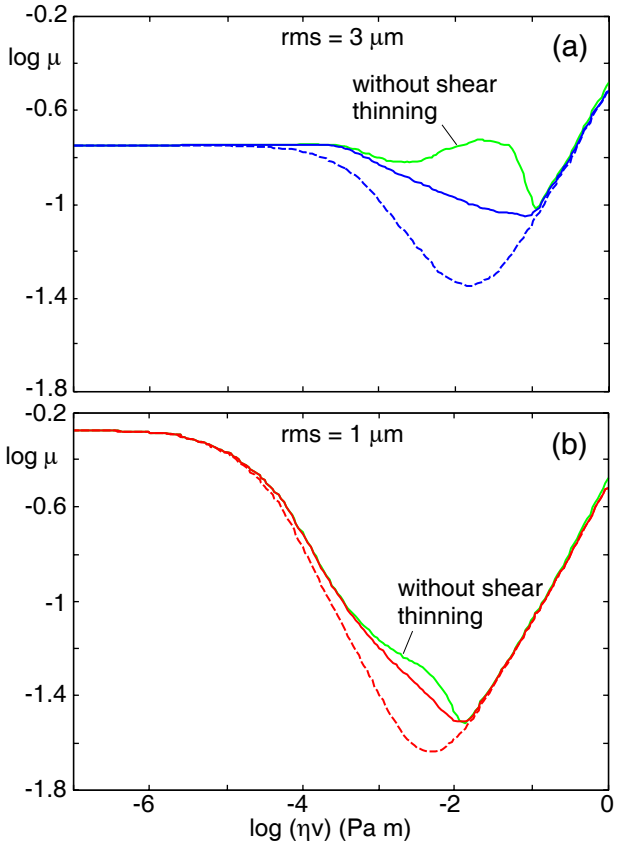

Fig. 13. (Colour on-line) The logarithm (with 10 as basis) of the friction coefficient as a function of the logarithm of the product ηv between the viscosity η and the velocity v for the (a) $h_{\rm rms} = 3\,\mu$m and (b) $h_{\rm rms} = 1\,\mu$m systems in fig. 9. The solid red and blue line represent the full theory while the dashed red and blue line represent the result with trivial frictional shear stress factors (both curves from fig. 9). The green lines represent the full theory without shear thinning.

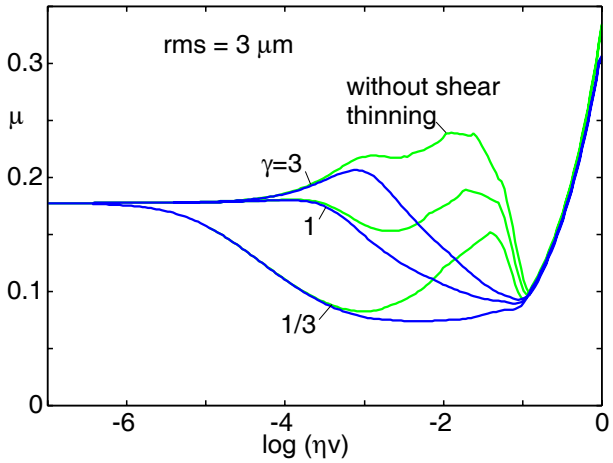

Fig. 14. (Colour on-line) The friction coefficient as a function of the logarithm (with 10 as basis) of the product ηv between the viscosity η and the velocity v for anisotropic surfaces with the Peklenik numbers $\gamma = 1/3$, 1 and 3. In all cases the angular average power spectrum is of the type shown in fig. 9 with $H = 0.8$ and $h_{\rm rms} = 3\,\mu$m. The blue lines represent the full theory with shear thinning, while the green lines represent the full theory without shear thinning.

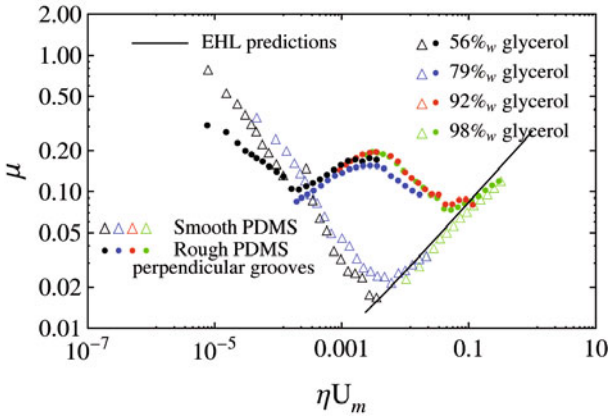

Fig. 15. The friction coefficient as a function of the product ηv between the viscosity η and the velocity v (log-log scale) for the contact between a smooth ball and a (nominally) flat rubber surface. The smooth and rough surfaces have rms roughness $h_{\rm rms} \approx 0.1$ and $\approx 10\,\mu$m, respectively.

erol and water) is not known to shear thin (or shear thin at very high shear rate) and this may effectively contribute towards the generation of the "bump" in the friction curve for the rough surface, in agreement with our theory predictions. On the very smooth surface no such bump is observed, which also agrees with our theory predictions (because the singularity u^{-1}, in the contribution to the frictional shear stress, is less important for smooth surfaces).

In fig. 16 we show the fraction of the load carried by the area of real contact (a) and the relative contact area (b), as a function of the logarithm of the product ηv for anisotropic surfaces with the Peklenik numbers $\gamma = 1/3$, 1 and 3. In all cases the angular average power spectrum is of the type shown in fig. 9 with $H = 0.8$ and $h_{\rm rms} = 3\,\mu$m and using the full theory with shear thinning. Note that in the mixed lubrication region, when γ decreases the area of real contact and the load carried by the contact regions decrease. This is the expected result because $\gamma < 1$ corresponds to surface roughness where the "groves" are aligned along the cylinder axis resulting in (pressurized) fluid trapped in the groves and in a reduced area of real contact and friction. On the other hand, for $\gamma > 1$, the groves are in the sliding direction and result in more effective fluid removal than for isotropic surface roughness. Note that this is only expected for the cylinder geometry: for a circular contact region both $\gamma > 1$ and $\gamma < 1$ result in enhanced fluid removal, as compared to the case of isotropic roughness ($\gamma = 1$), because of fluid squeeze-out (in the x- or y-direction) along the groves.

The study presented above does not include the deformations of the asperities by the fluid pressure but the asperities are only deformed by the contact pressure. We can estimate the influence of the fluid pressure on the asperity deformations using (28). In fig. 17 we show (a) the

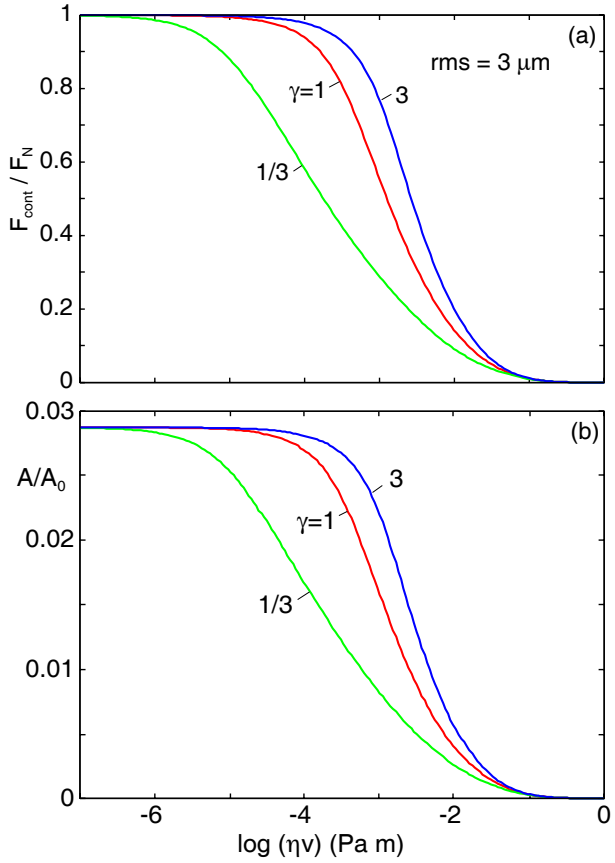

Fig. 16. (Colour on-line) The fraction of the load carried by the area of real contact (a) and the relative contact area (b), as a function of the logarithm (with 10 as basis) of the product ηv between the viscosity η and the velocity v for anisotropic surfaces with the Peklenik numbers $\gamma = 1/3$, 1 and 3. In all cases the angular average power spectrum is of the type shown in fig. 9 with $H = 0.8$ and $h_{\rm rms} = 3\,\mu$m. All cases using the full theory with shear thinning.

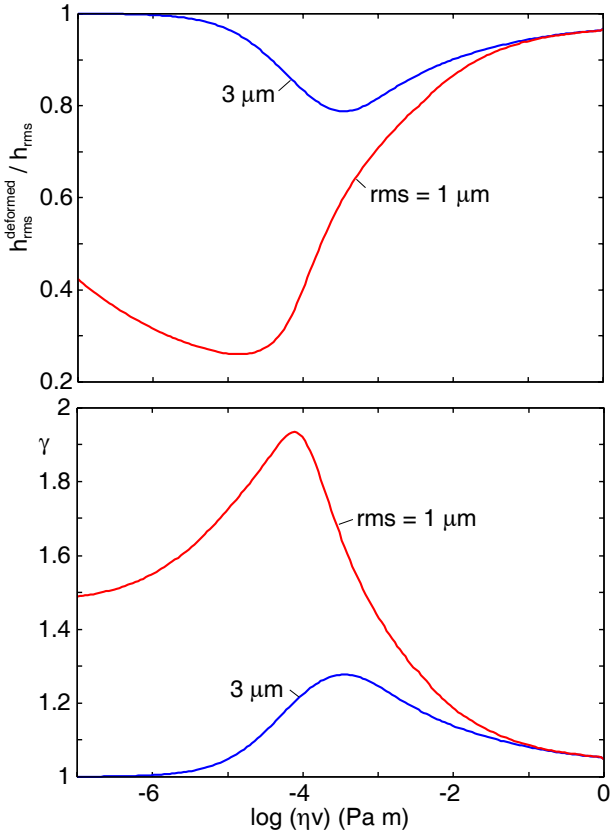

Fig. 17. (Colour on-line) The (a) root-mean-square roughness amplitude $h_{\rm rms}^{\rm deformed}$ (in units of the original (undeformed) $h_{\rm rms}$ roughness amplitude) and (b) the modified Peklenik factor as a function of the logarithm (with 10 as basis) of the product ηv between the viscosity η and the velocity v. For the $H = 0.8$ power spectra in fig. 9, with $h_{\rm rms} = 1\,\mu$m (red curve) and $3\,\mu$m (blue curve).

root-mean-square roughness amplitude $h_{\rm rms}^{\rm deformed}$ (in units of the original (undeformed) $h_{\rm rms}$ roughness amplitude), and (b) the Peklenik factor as a function of the logarithm (with 10 as basis) of the product ηv between the viscosity η and the velocity v. The results are for the surface with the $H = 0.8$ power spectra in fig. 9 with $h_{\rm rms} = 1\,\mu$m (red curve) and $3\,\mu$m (blue curve, see also [16]).

In fig. 18(a) we show the original (green lines, from fig. 9) and the modified (red lines and blue lines) surface roughness power spectra for the $H = 0.8$ power spectra in fig. 9 with $h_{\rm rms} = 1\,\mu$m (red curves) and $3\,\mu$m (blue curves). In fig. 18(b) we show for the same surface the Peklenik function $\gamma(q)$. The results shown are for all sliding velocities, but the individual lines are so closely spaced that they cannot be resolved. Only the region $q < 10^6\,{\rm m}^{-1}$ is shown as there is no modification of the power spectra for larger q. That is, the local fluid pressure only modifies (flattens) the long-wavelength roughness and, between those, mainly the long-wavelength roughness asperities with wave vector aligned with the sliding velocity [15]. This is illustrated schematically in fig. 19 where we show how the fluid flow deforms the big asperities (gray ellipses) while the small asperities remain unchanged (small black circles). The figure indicates the average shape of asperities; in reality asperities have fractal-like shape. Note that the deformations of the asperities is such as to facilitate the fluid flow (*i.e.*, to reduce the flow resistance).

One may include the fluid-pressure–induced modification of the surface roughness profile in the numerical study by repeating the fluid dynamics calculation with the modified power spectra (which will be different for each sliding velocity v_0) and the Peklenik function $\gamma(\zeta)$ (with $q = q_0\zeta$) shown in fig. 18. By performing this procedure several times (*i.e.*, several iterations) one can obtained a converged solution where the power spectra and Peklenik function (as a function of $q = q_0\zeta$) no longer change with each new iteration.

10.2 High-pressure system

We now consider an elastic cylinder (radius $R = 0.7\,$mm, elastic modulus $E = 3\,$MPa) sliding on a hard substrate in a fluid with viscosity $\eta = 12.5\,$Pa s. The cylinder has sur-

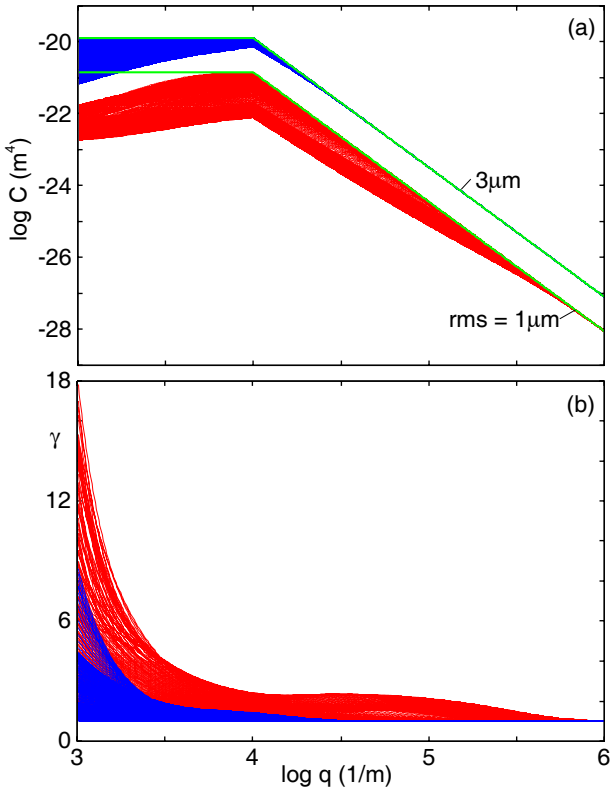

Fig. 18. (Colour on-line) (a) The original (green lines, from fig. 9) and the modified (red lines and blue lines) surface roughness power spectra for the $H = 0.8$ power spectra in fig. 9 with $h_{\rm rms} = 1\,\mu$m (red curves) and $3\,\mu$m (blue curves). (b) The Peklenik function $\gamma(q)$ for the same surfaces as in (a). Results shown for all sliding velocities ($10^{-6}\,$m/s $< v <$ 10 m/s) but the individual lines are so closely spaced that they cannot be resolved. Only the region $q < 10^6\,{\rm m}^{-1}$ is shown as there is no modification of the power spectra for larger q.

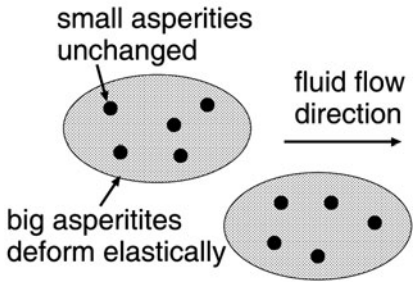

Fig. 19. The fluid flow deforms the big asperities (gray ellipses) while the small asperities remains unchanged (small black circles). The figure indicates the average shape of the asperities as in reality asperities have fractal-like shape.

face roughness with the power spectra shown in fig. 8 (blue curve), with the root-mean-square (rms) roughness $h_{\rm rms} = 0.3\,\mu$m. Figure 20 shows the friction coefficient as a function of the logarithm (with 10 as basis) of the product ηv between the viscosity η and the velocity v. The frictional shear stress in the area of real contact $\sigma_{\rm f} = 1.36\,$MPa and the load on the cylinder per unit length $F_{\rm N}/L = 200\,$N/m.

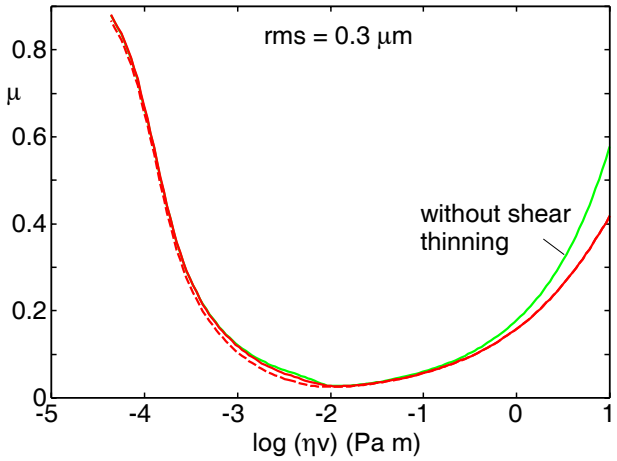

Fig. 20. (Colour on-line) The friction coefficient as a function of the logarithm (with 10 as basis) of the product ηv between the viscosity η and the velocity v. For an elastic cylinder (radius $R = 0.7\,$mm, elastic modulus $E = 3\,$MPa) sliding on a hard substrate in a fluid with viscosity $\eta = 12.5\,$Pa s. The cylinder has surface roughness with a power spectrum of the type shown in fig. 8 (blue curve), with the root-mean-square (rms) roughness $h_{\rm rms} = 0.3\,\mu$m. The frictional shear stress in the area of real contact $\sigma_{\rm f} = 1.36\,$MPa. The load on the cylinder per unit length $F_{\rm N}/L = 200\,$N/m. The static Hertz contact region has half-width $a_{\rm H} = 0.21\,$mm and the maximum and average Hertz contact pressure are $p_{\rm max} = 0.60\,$MPa and $p_{\rm av} = 0.47\,$MPa, respectively. The solid red line is the full theory while the dashed red line is the result with trivial friction flow factors. The green line is the full theory without shear thinning.

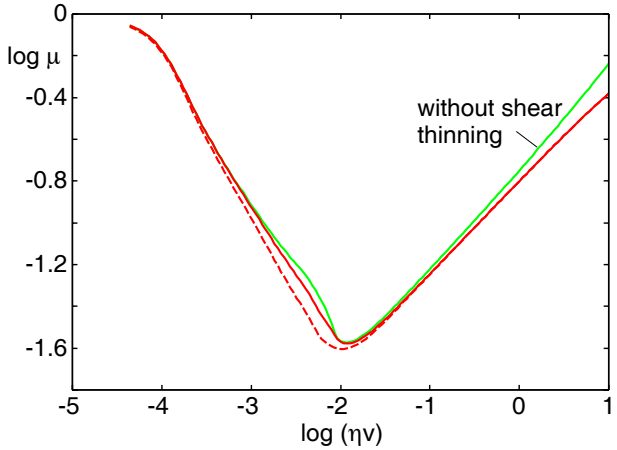

Fig. 21. (Colour on-line) The same data as in fig. 20 but with the logarithm (with 10 as basis) of the friction coefficient as a function of the logarithm of the product ηv.

The solid red line is the full theory while the dashed red is the result with trivial friction factors. The green lines is the full theory without shear thinning.

In fig. 21 we show the same data as in fig. 20 but with the logarithm (with 10 as basis) of the friction coefficient as a function of the logarithm of the product ηv.

In fig. 22 we show the friction coefficient as a function of the product ηv. The red curve is for the load

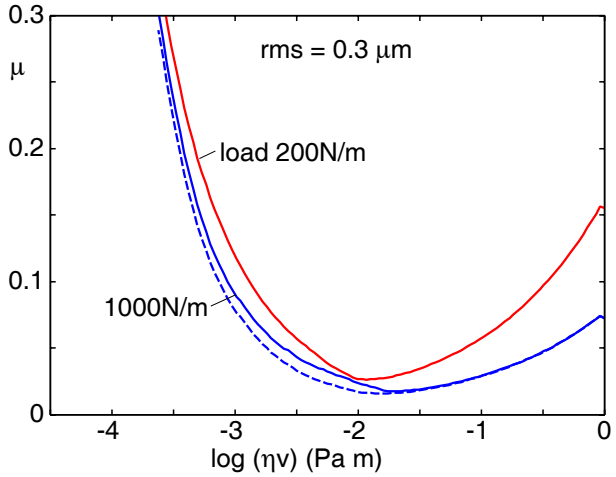

Fig. 22. (Colour on-line) The friction coefficient as a function of the logarithm (with 10 as basis) of the product ηv between the viscosity η and the velocity v. For an elastic cylinder (radius $R = 0.7\,\mathrm{mm}$, elastic modulus $E = 3\,\mathrm{MPa}$) sliding on a hard substrate in a fluid with viscosity $\eta = 12.5\,\mathrm{Pa\,s}$. The cylinder has surface roughness with a power spectra of the type shown in fig. 8 (blue curve), with the root-mean-square (rms) roughness $h_{\mathrm{rms}} = 0.3\,\mu\mathrm{m}$. The frictional shear stress in the area of real contact $\sigma_{\mathrm{f}} = 1.36\,\mathrm{MPa}$. Red curve: the load on the cylinder per unit length $F_{\mathrm{N}}/L = 200\,\mathrm{N/m}$ (from fig. 20). Blue curves: the load on the cylinder per unit length $F_{\mathrm{N}}/L = 1000\,\mathrm{N/m}$. The solid blue is the full theory while the dashed blue curve is the result with trivial friction flow factors. For the load $F_{\mathrm{N}}/L = 1000\,\mathrm{N/m}$ the static Hertz contact region has half-width $a_{\mathrm{H}} = 0.47\,\mathrm{mm}$ and the maximum and average Hertz contact pressure are $p_{\mathrm{max}} = 1.35\,\mathrm{MPa}$ and $p_{\mathrm{av}} = 1.06\,\mathrm{MPa}$, respectively.

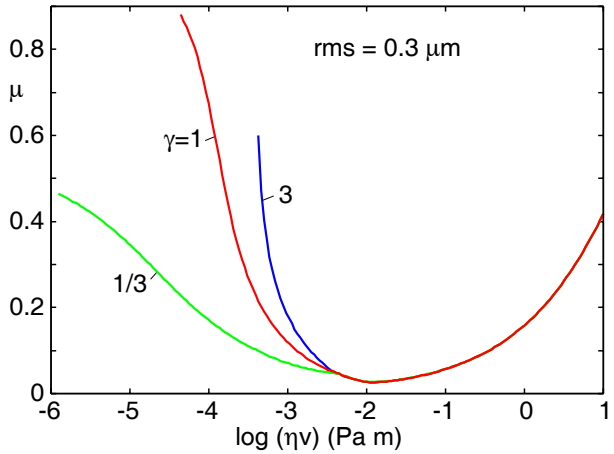

Fig. 23. (Colour on-line) The friction coefficient as a function of the logarithm (with 10 as basis) of the product ηv between the viscosity η and the velocity v for anisotropic surfaces with the Peklenik numbers $\gamma = 1/3$, 1 and 3. In all cases the angular average power spectrum is of the type shown in fig. 9 with $H = 1$ and $h_{\mathrm{rms}} = 0.3\,\mu\mathrm{m}$. All cases using the full theory with shear thinning.

(per unit length) on the cylinder $F_{\mathrm{N}}/L = 200\,\mathrm{N/m}$ (from fig. 20), while the the blue curves are for the load $F_{\mathrm{N}}/L = 1000\,\mathrm{N/m}$. The solid blue curve is the full theory while the dashed blue curve is the result with trivial friction factors. Note that in the hydrodynamic region the friction coefficient depends on the load F_{N} roughly like predicted by $\mu \sim \log(\eta v/F_{\mathrm{N}})$ but this scaling is not obeyed in the mixed lubrication velocity range. The nominal pressure in the (nominal) contact area when $F_{\mathrm{N}}/L = 1000\,\mathrm{N/m}$ (which is of order $\sim 1\,\mathrm{MPa}$) is typical for applications to syringes (between the ribs of the rubber stopper and the glass or polymer container), and the friction coefficient close to the minimum of the $\mu(v)$ curve is in good agreement with the measured friction coefficient [37].

Let us now consider anisotropic surfaces. In fig. 23 we show the friction coefficient as a function of the logarithm of ηv for anisotropic surfaces with the Peklenik numbers $\gamma = 1/3$, 1 and 3. Note that decreasing γ lowers the friction because of the (pressurized) fluid trapped in the groves of the roughness profile. As discussed before, this is the case for a cylinder geometry with the groves aligned along the cylinder axis. For the ball-on-flat configuration the effect of an anisotropic roughness is instead less predictable, since the fluid flow direction varies at different contact positions, resulting consequently in different removal rates of the fluid from the interface, and therefore in different frictional behaviors.

For the same systems as in fig. 23 we show in fig. 24 the fraction of the load carried by the area of real contact (a) and the relative contact area (b), as a function of the logarithm of the product ηv. It is remarkable that even for large contact area, most of the load is carried by the fluid. The reason is that at the lowest velocity the area of real contact is close to the percolation limit and fluid becomes trapped at the interface (there are no channels for fluid squeeze-out) and the fluid becomes highly compressed and carry most of the load. This effect is only observed when the load is so high that the (nominal) contact pressure becomes so large to cause the area of real contact to be close to the percolation threshold.

11 Summary and conclusion

We have studied the fluid flow at the interface between elastic solids with randomly rough surfaces. We have derived (approximate) analytical expressions for the fluid flow factors which enter in the equation describing the fluid flow, and for the frictional shear stress factors which enter in the equation for the frictional shear stress. Numerical results for a rubber cylinder with surface roughness sliding on a flat lubricated substrate, under "low" and "high" pressure conditions, have been presented and discussed. We have also discussed the role of the fluid-induced elastic deformations of the surface roughness profile.

One of the main problems at present in order to (accurately) calculate the friction force as a function

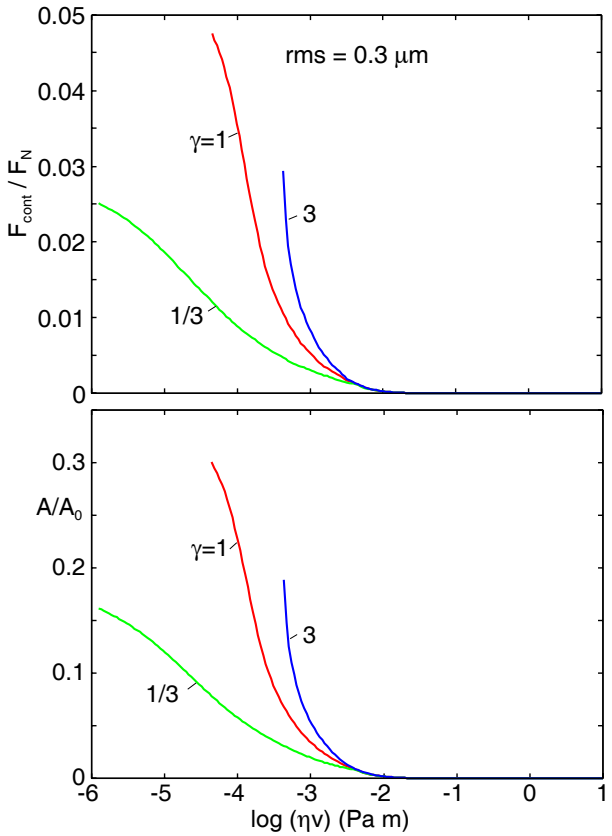

Fig. 24. (Colour on-line) The fraction of the load carried by the area of real contact (a) and the relative contact area (b), as a function of the logarithm (with 10 as basis) of the product ηv between the viscosity η and the velocity v for anisotropic surfaces with the Peklenik numbers $\gamma = 1/3$, 1 and 3. In all cases the angular average power spectrum is of the type shown in fig. 9 with $H = 1$ and $h_{\rm rms} = 0.3\,\mu$m. All curves have been calculated using the full theory with shear thinning.

of the sliding velocity (Stribeck curve), in particular in the mixed lubrication velocity region, is the rather limited knowledge about the rheological properties of thin confined lubricant films. We have demonstrated that even bulk shear thinning may strongly influence the friction, in particular in the transition region from hydrodynamic to mixed lubrication. Some knowledge about thin-film rheology has been gained from molecular dynamics studies [29], and from measurements using the surface forces apparatus [26, 38], but these studies do not cover the whole range of film thickness and velocities involved in most practical applications.

We thank G. Carbone for useful discussions. MS acknowledges Regione Puglia for having supported the research activity through the constitution of the TRASFORMA Laboratory Network cod. 28. This work, as part of the European Science Foundation EUROCORES Program FANAS, was supported from funds by the DFG and the EC Sixth Framework Program, under contract N ERAS-CT-2003-980409.

Appendix A. Perturbation calculation of flow factors

Here we derive an effective flow equation by integrating out the short-wavelength roughness. We first extend the result of Tripp by including the elastic deformations of the solid walls induced by the pressure in the fluid (see also [15]). We will assume that there is no real contact between the two solids, *i.e.*, a fluid film will separate the solid walls everywhere.

Appendix A.1. Flow factors for $\langle h^2\rangle/\bar{u}^2 \ll 1$

Assume that the surface roughness is given by the height coordinate $z = h(\mathbf{x})$. Let $\bar{u}$ be the average separation between the surfaces. We assume first $h/\bar{u} \ll 1$ and perform a perturbation expansion in the small parameter $h/\bar{u}$. Let us write the fluid pressure as

$$p = p_0 + p_1 + p_2 + \ldots, \tag{A.1}$$

where p_0 is the pressure to zero order in h (so that $p_0 = \langle p_0\rangle$), p_1 to first order in h and so on. Let $u(\mathbf{x}) = \bar{u}+u_1(\mathbf{x})+u_2(\mathbf{x})$ denote the local surface separation, where $\bar{u} = \langle u\rangle$ is the average separation ($\langle\ldots\rangle$ stands for ensemble averaging), $u_1 = h+\hat{K}p_1$ and $u_2 = \hat{K}(p_2-\langle p_2\rangle)$, where $h(\mathbf{x})$ denotes the surface roughness profile in the absence of elastic deformations with $\langle h\rangle = 0$, and $\hat{K}(p_1+p_2)$ denote the elastic deformation displacements of the walls due to the fluid pressure. Here $\hat{K}$ is an integral operator

$$\hat{K}p(\mathbf{x}) = \int {\rm d}^2x'\, K(\mathbf{x}-\mathbf{x}')p(\mathbf{x}').$$

In wave vector space the right-hand side of this equation becomes a product $K(q)p(\mathbf{q})$, where from the theory of elasticity $K(q) = -2/qE^*$, where $E^* = E/(1-\nu^2)$ (where E is Young's modulus and ν the Poisson ratio). Note that $\langle u_1\rangle = \langle u_2\rangle = 0$.

The fluid flow current is given by

$$\mathbf{J} = -\frac{u^3}{12\eta}\nabla p + \frac{1}{2}u\mathbf{v}.$$

Thus to second order in h we get

$$\mathbf{J} = -\frac{\bar{u}^3}{12\eta}\nabla(p_0+p_1+p_2) - \frac{3\bar{u}^2u_1}{12\eta}\nabla(p_0+p_1) - \frac{3(\bar{u}^2u_2+\bar{u}u_1^2)}{12\eta}\nabla p_0 + \frac{1}{2}(\bar{u}+u_1+u_2)\mathbf{v}. \tag{A.2}$$

The ensemble average of this equation gives

$$\langle\mathbf{J}\rangle = -\frac{\bar{u}^3}{12\eta}\nabla\langle p_0+p_1+p_2\rangle - \frac{3\bar{u}^2}{12\eta}\langle u_1\nabla p_1\rangle - \frac{3\bar{u}\langle u_1^2\rangle}{12\eta}\nabla p_0 + \frac{1}{2}\bar{u}\mathbf{v}, \tag{A.3}$$

where we have used that $\langle u_1\rangle = \langle u_2\rangle = 0$. Using that

$$\nabla\cdot\mathbf{J} = 0,$$

we get from (A.2) to zero order in h

$$\nabla^2 p_0 = 0.$$

The first-order contribution gives

$$-\frac{\bar u^3}{12\eta}\nabla^2 p_1 - \frac{3\bar u^2}{12\eta}\nabla\cdot(u_1\nabla p_0) + \frac{1}{2}\mathbf{v}\cdot\nabla u_1 = 0. \quad \text{(A.4)}$$

We define

$$p_1(\mathbf{q}) = \frac{1}{(2\pi)^2}\int \mathrm{d}^2x\, p_1(\mathbf{x})e^{-i\mathbf{q}\cdot\mathbf{x}}$$
$$p_1(\mathbf{x}) = \int \mathrm{d}^2q\, p_1(\mathbf{q})e^{i\mathbf{q}\cdot\mathbf{x}}$$

and similar for $h(\mathbf{x})$. Substituting these results in (A.4) gives

$$\frac{\bar u^3}{12\eta}q^2 p_1(\mathbf{q}) - \frac{3\bar u^2}{12\eta}u_1(\mathbf{q})(i\mathbf{q})\cdot\nabla p_0 + \frac{1}{2}\mathbf{v}\cdot(i\mathbf{q})u_1(\mathbf{q}) = 0$$

or using that $u_1(\mathbf{q}) = h(\mathbf{q}) + K(q)p_1(\mathbf{q})$,

$$p_1(\mathbf{q}) = \frac{1}{S(\mathbf{q})}\left(\frac{3}{\bar u q^2}(i\mathbf{q})\cdot\nabla p_0 - \frac{6\eta}{\bar u^3 q^2}\mathbf{v}\cdot(i\mathbf{q})\right)h(\mathbf{q}) \quad \text{(A.5)}$$

where

$$S(\mathbf{q}) = 1 - \frac{3}{\bar u q^2}K(q)(i\mathbf{q})\cdot\nabla p_0 + \frac{6\eta}{\bar u^3 q^2}K(q)(i\mathbf{q})\cdot\mathbf{v}. \quad \text{(A.6)}$$

Thus we get

$$u_1(\mathbf{q}) = h(\mathbf{q}) + K(q)p_1(\mathbf{q}) = h(\mathbf{q})/S(\mathbf{q}). \quad \text{(A.7)}$$

Next, note that

$$\begin{aligned}
&\langle h(\mathbf{q})h(\mathbf{q}')\rangle = \\
&\frac{1}{(2\pi)^4}\int \mathrm{d}^2x\mathrm{d}^2x'\,\langle h(\mathbf{x})h(\mathbf{x}')\rangle e^{i\mathbf{q}\cdot\mathbf{x}+i\mathbf{q}'\cdot\mathbf{x}'} = \\
&\frac{1}{(2\pi)^4}\int \mathrm{d}^2x\mathrm{d}^2x'\,\langle h(\mathbf{x}-\mathbf{x}')h(\mathbf{0})\rangle e^{i\mathbf{q}\cdot\mathbf{x}+i\mathbf{q}'\cdot\mathbf{x}'} = \\
&\frac{1}{(2\pi)^4}\int \mathrm{d}^2x\mathrm{d}^2x'\,\langle h(\mathbf{x}-\mathbf{x}')h(\mathbf{0})\rangle e^{i\mathbf{q}\cdot(\mathbf{x}-\mathbf{x}')+i(\mathbf{q}'+\mathbf{q})\cdot\mathbf{x}'} = \\
&\frac{1}{(2\pi)^4}\int \mathrm{d}^2x\mathrm{d}^2x'\,\langle h(\mathbf{x})h(\mathbf{0})\rangle e^{i\mathbf{q}\cdot\mathbf{x}+i(\mathbf{q}'+\mathbf{q})\cdot\mathbf{x}'} = \\
&\frac{1}{(2\pi)^2}\int \mathrm{d}^2x\,\langle h(\mathbf{x})h(\mathbf{0})\rangle e^{i\mathbf{q}\cdot\mathbf{x}}\delta(\mathbf{q}+\mathbf{q}') = \\
&C(\mathbf{q})\delta(\mathbf{q}+\mathbf{q}'). \quad \text{(A.8)}
\end{aligned}$$

Using this equation and (A.5) and (A.7) gives

$$\begin{aligned}
\langle u_1\nabla p_1\rangle &= \int \mathrm{d}^2q\mathrm{d}^2q'\,(i\mathbf{q}')\langle u_1(\mathbf{q})p_1(\mathbf{q}')\rangle e^{i(\mathbf{q}+\mathbf{q}')\cdot\mathbf{x}} \\
&= \int \mathrm{d}^2q\,\frac{C(\mathbf{q})}{|S(\mathbf{q})|^2}\frac{\mathbf{q}\mathbf{q}}{q^2}\cdot\left(\frac{6\eta}{\bar u^3}\mathbf{v} - \frac{3}{\bar u}\nabla p_0\right). \quad \text{(A.9)}
\end{aligned}$$

Substituting this result in (A.3) gives

$$\langle\mathbf{J}\rangle = A(\bar u)\nabla\bar p + B(\bar u)\mathbf{v}, \quad \text{(A.10)}$$

where $\bar p = \langle p_0 + p_1 + p_2\rangle$, and where the 2×2 matrices A and B can be written as $A = -\bar u^3\phi_{\rm p}/(12\eta)$ and $B = \bar u/2 + h_{\rm rms}\phi_{\rm s}/2$ with the flow factor matrices

$$\begin{aligned}
\phi_{\rm p} &= 1 + \frac{3}{\bar u^2}\left(\langle u_1^2\rangle - 3\int \mathrm{d}^2q\,\frac{C(\mathbf{q})}{|S(\mathbf{q})|^2}\frac{\mathbf{q}\mathbf{q}}{q^2}\right) \\
&= 1 + \frac{3\langle u_1^2\rangle}{\bar u^2}(1 - 3\tilde D), \quad \text{(A.11)}
\end{aligned}$$

and

$$\phi_{\rm s} = -\frac{3}{\bar u h_{\rm rms}}\int \mathrm{d}^2q\,\frac{C(\mathbf{q})}{|S(\mathbf{q})|^2}\frac{\mathbf{q}\mathbf{q}}{q^2} = -\frac{3\langle u_1^2\rangle}{\bar u h_{\rm rms}}\tilde D. \quad \text{(A.12)}$$

Here we have defined the 2×2 matrix

$$\tilde D = \frac{\int \mathrm{d}^2q\,\tilde C(\mathbf{q})\mathbf{q}\mathbf{q}/q^2}{\int \mathrm{d}^2q\;\tilde C(\mathbf{q})},$$

where $\tilde C(\mathbf{q}) = C(\mathbf{q})/|S(\mathbf{q})|^2$ [15]. In deriving (A.10) we have used that to order h^2 one can replace terms like $h^2\nabla p_0$ with $h^2\nabla\bar p$. Note also that

$$\begin{aligned}
\langle u_1^2\rangle &= \int \mathrm{d}^2q\mathrm{d}^2q'\langle u_1(\mathbf{q})u_1(\mathbf{q}')\rangle = \int \mathrm{d}^2q\mathrm{d}^2q'\,\frac{\langle h(\mathbf{q})h(\mathbf{q}')\rangle}{S(\mathbf{q})S(\mathbf{q}')} \\
&= \int \mathrm{d}^2q\frac{C(\mathbf{q})}{|S(\mathbf{q})|^2} = \int \mathrm{d}^2q\,\tilde C(\mathbf{q}).
\end{aligned}$$

In the derivation above we have assumed $h_{\rm rms}/\bar u \ll 1$. However, it is likely that the final result is valid under a more general condition, namely that the difference in the corrugation of the substrate and the deformed bottom surface of the block is small compared to $\bar u$; that is, $\langle u_1^2\rangle/\bar u^2 \ll 1$. For elastically very soft solids such as gelatin, this condition may be satisfied under quite general conditions.

Note that including the fluid-pressure–induced (short wavelength) deformations of the surface roughness profile is equivalent to using a deformed surface profile obtained by replacing $h(\mathbf{q})$ with $\tilde h(\mathbf{q}) = h(\mathbf{q})/S(\mathbf{q})$. The resulting surface will be anisotropic with the asperities deformed so that they are on the average elongated along the fluid flow direction. We will refer to the surface roughness anisotropy, resulting from the elastic deformations (at the roughness length scale) induced by the fluid flow, as dynamically induced anisotropy in contrast to the static surface roughness anisotropy, which may prevail before contact between the solids [15].

Appendix A.2. Integrating out length scales

Let us assume that the (effective) viscosity η depends on the interfacial separation $u(\mathbf{x})$ and the velocity v. Let us write $A = -u^3/[12\eta(u,v)]$ and $B = u/2$. In this case the fluid flow current is given by

$$\mathbf{J} = A(u)\nabla p + B(u)\mathbf{v}$$

or on index form (sum over repeated indices is implicitly understood)

$$J_i = A_{ij}(u)\partial_j p + B_{ij}(u)v_j.$$

Thus to second order in h we get

$$\begin{aligned}\mathbf{J} &= A(\bar{u})\nabla(p_0+p_1+p_2)\\ &+A'(\bar{u})u_1\nabla(p_0+p_1)+\left(A'(\bar{u})u_2+\frac{1}{2}A''(\bar{u})u_1^2\right)\nabla p_0\\ &+\left(B(\bar{u})+B'(\bar{u})(u_1+u_2)+\frac{1}{2}B''(\bar{u})u_1^2\right)\mathbf{v}. \qquad (A.13)\end{aligned}$$

The ensemble average of this equation gives

$$\begin{aligned}\langle\mathbf{J}\rangle &= A(\bar{u})\nabla\langle p_0+p_1+p_2\rangle\\ &+A'(\bar{u})\langle u_1\nabla p_1\rangle+\frac{1}{2}A''(\bar{u})\langle u_1^2\rangle\nabla p_0\\ &+\left(B(\bar{u})+\frac{1}{2}B''(\bar{u})\langle u_1^2\rangle\right)\mathbf{v}, \qquad (A.14)\end{aligned}$$

where we have used that $\langle u_1\rangle = \langle u_2\rangle = 0$. Using that

$$\nabla\cdot\mathbf{J} = 0,$$

we get from (A.13) to zero-order in h

$$A_{ij}\partial_i\partial_j p_0 = 0.$$

The first-order contribution gives

$$A_{ij}\partial_i\partial_j p_1 + A'_{ij}\partial_i(u_1\partial_j p_0) + B'(\bar{u})\partial_i u_1 v_j = 0. \qquad (A.15)$$

We define

$$\begin{aligned}p_1(\mathbf{q}) &= \frac{1}{(2\pi)^2}\int \mathrm{d}^2x\, p_1(\mathbf{x})e^{-i\mathbf{q}\cdot\mathbf{x}},\\ p_1(\mathbf{x}) &= \int \mathrm{d}^2q\, p_1(\mathbf{q})e^{i\mathbf{q}\cdot\mathbf{x}}\end{aligned}$$

and similar for $h(\mathbf{x})$. Substituting these results in (A.15) gives

$$A_{ij}(-q_iq_j)p_1(\mathbf{q})+A'_{ij}u_1(\mathbf{q})(iq_i)\partial_j p_0+B'_{ij}(iq_i)u_1(\mathbf{q})v_j = 0, \qquad (A.16)$$

or, using that $u_1(\mathbf{q}) = h(\mathbf{q}) + K(q)p_1(\mathbf{q})$,

$$p_1(\mathbf{q}) = S^{-1}(A_{ij}q_iq_j)^{-1}\left(A'_{ij}iq_i\partial_j p_0 + B'_{ij}iq_iv_j\right)h(\mathbf{q}), \qquad (A.17)$$

where

$$S(\mathbf{q}) = 1 - K(q)(A_{ij}q_iq_j)^{-1}\left(A'_{ij}iq_i\partial_j p_0 + B'_{ij}iq_iv_j\right). \qquad (A.18)$$

Thus we get

$$u_1(\mathbf{q}) = h(\mathbf{q}) + K(q)p_1(\mathbf{q}) = S^{-1}h(\mathbf{q}). \qquad (A.19)$$

Using (A.8) and (A.17) and (A.19) gives

$$\begin{aligned}\langle u_1\nabla p_1\rangle &= \int \mathrm{d}^2q\mathrm{d}^2q'\,(i\mathbf{q}')\langle u_1(\mathbf{q})p_1(\mathbf{q}')\rangle e^{i(\mathbf{q}+\mathbf{q}')\cdot\mathbf{x}}\\ &= -\int \mathrm{d}^2q\,\frac{C(\mathbf{q})}{|S(\mathbf{q})|^2}\frac{\mathbf{qq}}{A_{ij}q_iq_j}\cdot\left(A'\nabla p_0 + B'\mathbf{v}\right). \qquad (A.20)\end{aligned}$$

If we denote

$$F = \int \mathrm{d}^2q\,\frac{C(\mathbf{q})}{|S(\mathbf{q})|^2}\frac{\mathbf{qq}}{A_{ij}q_iq_j} \qquad (A.21)$$

then using (A.14) and (A.20) gives

$$\begin{aligned}\langle\mathbf{J}\rangle &= \left(A - A'FA' + \frac{1}{2}A''\langle u_1^2\rangle\right)\nabla\bar{p}\\ &+\left(B - A'FB' + \frac{1}{2}B''\langle u_1^2\rangle\right)\mathbf{v}, \qquad (A.22)\end{aligned}$$

where $\bar{p} = \langle p_0+p_1+p_2\rangle$. In deriving (A.22) we have used that to order h^2 one can replace terms like $h^2\nabla p_0$ with $h^2\nabla\bar{p}$. Note also that

$$\begin{aligned}\langle u_1^2\rangle &= \int \mathrm{d}^2q\mathrm{d}^2q'\langle u_1(\mathbf{q})u_1(\mathbf{q}')\rangle = \int \mathrm{d}^2q\mathrm{d}^2q'\frac{\langle h(\mathbf{q})h(\mathbf{q}')\rangle}{S(\mathbf{q})S(\mathbf{q}')}\\ &= \int \mathrm{d}^2q\frac{C(\mathbf{q})}{|S(\mathbf{q})|^2} = \int \mathrm{d}^2q\,\tilde{C}(\mathbf{q}).\end{aligned}$$

If we assume $A = -u^3/(12\eta_0)$ (where η_0 is independent of u) and $B = u/2$ then (A.22) takes the form

$$\langle\mathbf{J}\rangle = -\frac{\bar{u}^3}{12\eta_0}\phi_{\mathrm{p}}\nabla\bar{p} + \frac{1}{2}\bar{u}\mathbf{v} + \frac{1}{2}h_{\mathrm{rms}}\phi_{\mathrm{s}}\mathbf{v},$$

with the flow factor matrices ϕ_{p} and ϕ_{s} given by (A.11) and (A.12), respectively.

In the calculation above we derived the pressure and shear flow factors to first order in $\langle u_1^2\rangle/\bar{u}^2$. We can extend the theory to higher order in $\langle u_1^2\rangle/\bar{u}^2$ by using a Renormalization Group (RG) type of procedure. Thus we will eliminate or integrate out the surface roughness components in steps and obtain a set of RG flow equations describing how the effective fluid equation evolves as more and more of the surface roughness components are eliminated.

Assume that after eliminating all the surface roughness components with wave vector $|\mathbf{q}| = q > \zeta q_0$ the fluid current (given by (1)) takes the form

$$\mathbf{J} = A(\bar{u})\nabla p + B(\bar{u})\mathbf{v}, \qquad (A.23)$$

where A and B are 2×2 matrices. We now add to $\bar{u}$ a small amount of roughness

$$h = \int_{(\zeta-\Delta\zeta)q_0<q<\zeta q_0} \mathrm{d}^2q\,h(\mathbf{q})e^{i\mathbf{q}\cdot\mathbf{x}}. \qquad (A.24)$$

This will result in an interfacial separation

$$u(\mathbf{x}) = \bar{u} + u_1(\mathbf{x}) + u_2(\mathbf{x}),$$

where $u_1 = h + \hat{K}p_1$ and $u_2 = \hat{K}(p_2 - \langle p_2\rangle)$, where p_1 and p_2 are the changes in the fluid pressure to first and second order in h. Consider now the current

$$\mathbf{J} = A(\bar{u}+u_1+u_2)\nabla p + B(\bar{u}+u_1+u_2)\mathbf{v}.$$

Following the derivation presented above we obtain to second order in h the current (from here on we denote $\bar{u} = u$ for simplicity)

$$\langle \mathbf{J} \rangle = \left(A(u) + \frac{1}{2}\langle u_1^2 \rangle A''(u) - \langle u_1^2 \rangle A'(u) M A'(u) \right) \nabla \bar{p} + \left(B(u) + \frac{1}{2}\langle u_1^2 \rangle B''(u) - \langle u_1^2 \rangle A'(u) M B'(u) \right) \mathbf{v}, \tag{A.25}$$

where $M = F/\langle u_1^2 \rangle$. Note that this equation has the same general form as the original equation (A.23). If we denote the matrices A and B in the original equation (A.23) as $A(u,\zeta)$ and $B(u,\zeta)$ to indicate that these were the matrices obtained after eliminating all wave vector components of h with $q > \zeta q_0$, then the new matrices obtained by eliminating the additional roughness with wave vectors between $(\zeta - \Delta\zeta)q_0 < q < \zeta q_0$ become

$$A(u,\zeta - \Delta\zeta) = A(u,\zeta) + \frac{1}{2}\langle u_1^2 \rangle A''(u,\zeta) - \langle u_1^2 \rangle A'(u,\zeta) M A'(u,\zeta), \tag{A.26}$$

$$B(u,\zeta - \Delta\zeta) = B(u,\zeta) + \frac{1}{2}\langle u_1^2 \rangle B''(u,\zeta) - \langle u_1^2 \rangle A'(u,\zeta) M B'(u,\zeta). \tag{A.27}$$

Since $\Delta\zeta$ is small we can expand the left-hand side to linear order in $\Delta\zeta$. Furthermore note that

$$\frac{\langle u_1^2 \rangle}{\Delta\zeta} = \frac{1}{\Delta\zeta} \int_{(\zeta-\Delta\zeta)q_0 < q < \zeta q_0} \mathrm{d}^2 q\, \tilde{C}(\mathbf{q}) = \frac{1}{\Delta\zeta} \int_{(\zeta-\Delta\zeta)q_0}^{\zeta q_0} \mathrm{d}q q \int_0^{2\pi} \mathrm{d}\phi\, \tilde{C}(q\cos\phi, q\sin\phi) = \zeta q_0^2 \int_0^{2\pi} \mathrm{d}\phi\, \tilde{C}(\zeta q_0 \cos\phi, \zeta q_0 \sin\phi) = -\zeta^{-1} H(u,\zeta), \tag{A.28}$$

where

$$H(u,\zeta) = -q^2 \int \mathrm{d}\phi\, \tilde{C}(\mathbf{q}), \tag{A.29}$$

$q = q_0\zeta$, $\mathbf{q} = q(\cos\phi, \sin\phi)$ and where the integral is from 0 to 2π. We also get

$$M = \frac{\int \mathrm{d}\phi\, \tilde{C}(\mathbf{q}) \mathbf{q}\mathbf{q} (A_{ij} q_i q_j)^{-1}}{\int \mathrm{d}\phi\, \tilde{C}(\mathbf{q})}. \tag{A.30}$$

In these equations $\tilde{C} = C(\mathbf{q})/|S(\mathbf{q})|^2$ with

$$S(\mathbf{q}) = 1 - iK(q)(A_{ij} q_i q_j)^{-1} \mathbf{q} \cdot (A' \nabla p_0 + B' \mathbf{v}), \tag{A.31}$$

with $K(q) = -2/qE^*$. From (A.26), (A.27) and (A.28) we get

$$\frac{\partial A}{\partial \zeta} = \left[\frac{1}{2} A''(u,\zeta) - A'(u,\zeta) M(u,\zeta) A'(u,\zeta) \right] \zeta^{-1} H(u,\zeta), \tag{A.32}$$

$$\frac{\partial B}{\partial \zeta} = \left[\frac{1}{2} B''(u,\zeta) - A'(u,\zeta) M(u,\zeta) B'(u,\zeta) \right] \zeta^{-1} H(u,\zeta). \tag{A.33}$$

These equations together with (A.25) show how the equation for the flow current evolves as more and more roughness is included in the analysis. The macroscopic flow current (corresponding to $\zeta = 1$) is given by (A.23) with $A = A(u,1)$ and $B = B(u,1)$. The appropriate boundary condition to be used when integrating (A.32) and (A.33) are that at the shortest length scale (corresponding to the magnification ζ_1) $A(u,\zeta_1) = -u^3/[12\eta(u,v)]$ and $B(u,\zeta_1) = u/2$. In addition we need boundary conditions along the u-axis. These are that $A = B = 0$ for $u = 0$ and $A = -u^3/[12\eta_0]$ and $B = u/2$ as $u \to \infty$, since for very large separation the roughness will have a negligible influence on the fluid flow.

Since the magnification ζ may span many decades in length scale (say from nanometer to mm) it is for numerical purposes convenient to introduce $\mu = \log(\zeta)$. Thus if ζ varies from 1 to, say, 10^6, μ will vary from 0 to ≈ 14. We now consider all our fields as a function of μ rather than ζ and get

$$\frac{\partial A}{\partial \mu} = \left[\frac{1}{2} A''(u,\mu) - A'(u,\mu) M(u,\mu) A'(u,\mu) \right] H(u,\mu) \tag{A.34}$$

$$\frac{\partial B}{\partial \mu} = \left[\frac{1}{2} B''(u,\mu) - A'(u,\mu) M(u,\mu) B'(u,\mu) \right] H(u,\mu). \tag{A.35}$$

If we neglect elastic deformation (*i.e.*, $K(q) = 0$) and assume that the rough surface has isotropic statistical properties, then $A_{ij} = \delta_{ij} A(u,\zeta)$ and $B_{ij} = \delta_{ij} B(u,\zeta)$. Thus from (A.30) $M_{ij} = \delta_{ij}[2A(u,\zeta)]^{-1}$ and

$$H = -q^2 \int \mathrm{d}\phi C(q) = \zeta \frac{\mathrm{d}}{\mathrm{d}\zeta} \langle h^2 \rangle_\zeta,$$

substituting these relations into (A.32) and (A.33) gives

$$\frac{\partial A}{\partial \zeta} = \frac{1}{2} \left[A''(u,\zeta) - \frac{[A'(u,\zeta)]^2}{A(u,\zeta)} \right] \frac{\mathrm{d}}{\mathrm{d}\zeta} \langle h^2 \rangle_\zeta \tag{A.36}$$

$$\frac{\partial B}{\partial \zeta} = \frac{1}{2} \left[B''(u,\zeta) - \frac{A'(u,\zeta) B'(u,\zeta)}{A(u,\zeta)} \right] \frac{\mathrm{d}}{\mathrm{d}\zeta} \langle h^2 \rangle_\zeta. \tag{A.37}$$

As shown in ref. [14] it is easy to solve these equations using perturbation theory to arbitrary order in the surface roughness amplitude h. Since $A \to u^3/(12\eta_0)$ and $\langle h^2 \rangle_\zeta \to 0$ as $\zeta \to \zeta_1$ we can write

$$A(u,\zeta) = u^3/(12\eta_0) + a_1(u)\langle h^2 \rangle_\zeta + a_2(u)\langle h^2 \rangle_\zeta^2 + \dots. \tag{A.38}$$

Since $B \to u/2$ and $\langle h^2 \rangle_\zeta \to 0$ as $\zeta \to \zeta_1$ we can write

$$B(u,\zeta) = u/2 + b_1(u)\langle h^2 \rangle_\zeta + b_2(u)\langle h^2 \rangle_\zeta^2 + \dots. \tag{A.39}$$

Appendix B. Solution algorithm

Equations (30), (32), (36) (for $\zeta = 1$), (40) and (41) have been solved (numerically) with two different approaches depending on the lubrication regime (*i.e.* the sliding velocity) corresponding to the calculation contact conditions. For our problem we adapted the BLP and MHLS algorithms successfully applied in ref. [32] for the resolution of the mixed-elastohydrodynamic ball-on-flat lubrication problem. Two different numerical procedures are required due to the different analytical character of the system of equations under investigation at different lubrication conditions (see also ref. [32]). The computational domain is discretized with a constant grid size δ_x. Both numerical approaches require the discretization of the elastic integral (40)

$$\bar{u}_i = u_0 + f_i + \sum_h \left(D_i^h - D_0^h\right) p_h, \qquad \text{(B.1)}$$

where $\bar{u}_i$ is the separation at the grid point (i), u_0 is the central separation, f_i is the undeformed shape of the contact and D_i^h is the discrete elastic kernel, with the translational invariance and symmetry property $D_i^h = D_0^{|h-i|}$. We use the convergence criteria

$$N^{1/2} \frac{\sqrt{\sum_i \left(s_i^n - s_i^{n-1}\right)^2}}{\sum_i \left|s_i^{n-1}\right|} < \varepsilon_s,$$

where s_i^n is $\bar{u}_i^n$ or $p_{\mathrm{s},i}^n$ or $p_{\mathrm{f},i}^n$ (in this appendix B we denote p_{fluid} as p_{f} and p_{solid} as p_{s}).

Appendix B.1. BLP for boundary lubrication

In the boundary regime, the effect of the fluid on the contact behavior is almost negligible. Thus, the solution of the dry contact problem will dominate the solution of the complete problem. In this case, the main algorithm loop is shown in fig. 25.

The BLP is an iterative contact solver (m-index loop) connected to a successive under-relaxation (SUR) process for the numerical convergence error dumping. To initialize the calculation, a Hertzian contact pressure, or a solution from a different velocity run can be used. In each iteration, the fluid solver updates the fluid pressure with the actual approximation $[p_{\mathrm{f},i}^m]'$ from the previous separation $\bar{u}_i^{m-1}$. After convergence check and under-relaxation of the fluid pressure (with α_f in the range $= 10^{-1}$ to 10^{-3}, the higher for smaller roughness), the load conservation is applied by rescaling fluid and solid pressure and updating the central separation. With the scaled pressure fields, the elastic integral is performed, followed by a convergence error check and under-relaxation of the actual separation approximation (with α_u in the range $= 10^{-1}$ to 10^{-3}, the higher for smaller roughness). Finally, from the relaxed separation, the solid pressure is updated and under-relaxed ($\alpha_c = 0.5$), and the load conservation is performed again by scaling the pressure fields. In our calculations, a convergence separation error of 10^{-5} and a convergence fluid pressure error of 10^{-4} were used.

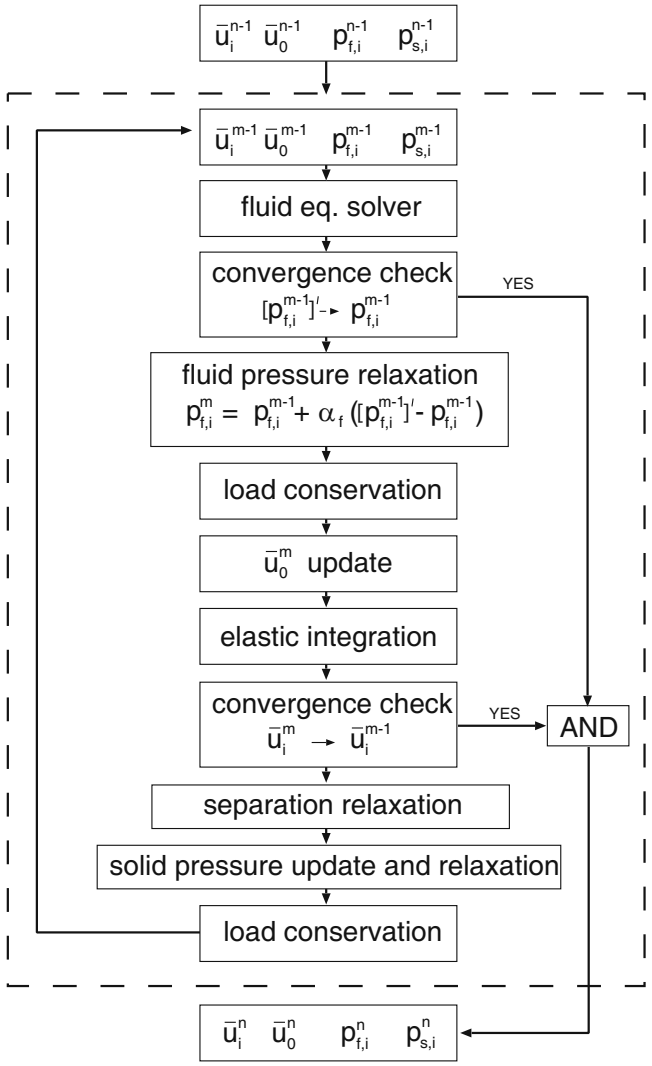

Fig. 25. BLP main loop.

The fluid solver (the l-index loop, inside the m-index loop) is an iterative solver based on the finite difference method to discretize (30), by means of central second-order difference for both sides of the equality. The error relaxation is achieved by Gauss Seidel (GS) sweeps

$$E_i \left[p_{\mathrm{f},i}^l\right]' = -\left(A_i \left[p_{\mathrm{f},i-1}^l\right]' + B_i p_{\mathrm{f},i+1}^l\right) + L_i,$$

if $p_{\mathrm{f},i}^{l-1} > 0$, or $[p_{\mathrm{f},i}^l]' = 0$ if $p_{\mathrm{f},i}^{l-1} \leq 0$. Here $p_{\mathrm{f},i}^{l-1=0} = p_{\mathrm{f},i}^{m-1}$. For SUR

$$p_{\mathrm{f},i}^l = p_{\mathrm{f},i}^{l-1} + \alpha \left(\left[p_{\mathrm{f},i}^l\right]' - p_{\mathrm{f},i}^{l-1}\right),$$

where α is generally in the range 0.6 to 0.8. The l-index loop is stopped after reaching a convergence error of 10^{-7}. The calculation of frictional fluid stress is trivial. For the asperity-asperity interaction numerical approach, see ref. [34].

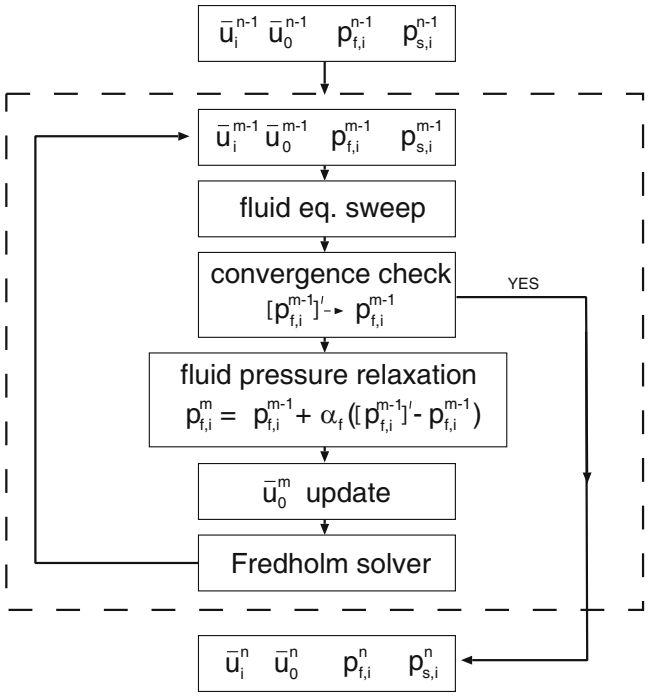

Fig. 26. MHLS main loop.

Appendix B.2. MHLS for mixed and hydrodynamic lubrication

In the mixed and hydrodynamic regimes the asperities contact plays a minor role because of the increased separation due to the higher fluid pressure. In this case the BLP algorithm is not able to relax the residuals, and the BLP procedure starts to diverge as soon as the fluid pressure becomes of the same order as solid pressure. This is a consequence of the non-linear coupling between the fluid pressure and the separation in the lubricant equation (30), that is not adequately handled in the BLP method. We now briefly describe the MHLS algorithm (see fig. 26) which is able to handle this situation.

The algorithm is an iterative solver of the Reynolds equation coupled with the asperity interaction problem reformulated as a Fredholm problem. For the mixed and hydrodynamic range, the complete problem solution is driven (or dominated) by the fluid equation. For large separation (hydrodynamic range), the MHLS becomes simply an elastohydrodynamic lubrication (EHL) solver. The algorithm requires input solution fields (*e.g.* from a previously obtained BLP solution, or simply using a Hertzian-like fluid pressure) in order to initialize the system. The relevant features are the Reynolds sweep algorithm (RSA), the central separation updater (CSU) and the Fredholm solver (FS).

The RSA updates the fluid pressure solution by one-sweep-relaxing of the residuals of the Reynolds equation. By considering the general m-iteration, the residuals of the fluid equation take the form

$$L_i^m = \bar{\phi}_{s,i+1}^m \bar{u}_{i+1}^m - \bar{\phi}_{s,i-1}^m \bar{u}_{i-1}^m - \left[A_i^m p_{f,i-1}^m + B_{ij}^m p_{f,i+1}^m + E_{ij}^m p_{f,i}^m\right], \tag{B.2}$$

where (30) was discretized by means of second-order central difference scheme for both sides of the equality, and we have defined $\bar{\phi}_s = 1 + \frac{h_{\rm rms}}{\bar{u}}\phi_s$. The coefficients of (B.2) are

$$A_i^m = \left(\phi_p \bar{u}^3\right)_{i-1/2}^m \frac{2}{\lambda \delta_x}, \qquad B_i^m = \left(\phi_p \bar{u}^3\right)_{i+1/2}^m \frac{2}{\lambda \delta_x},$$
$$E_i^m = -\frac{2}{\lambda \delta_x}\left[\left(\phi_p \bar{u}^3\right)_{i-1/2}^m + \left(\phi_p \bar{u}^3\right)_{i+1/2}^m\right] \tag{B.3}$$

and implicitly depend on the fluid solution (through the elastic deformation coupling and the flow factors separation dependence). $\lambda = 6\eta_0 v_0$. The fluid pressure is updated by a Newton-Rapson (NR) step

$$\sum_a \frac{\partial L_i^{m-1}}{\partial p_{f,a}}\left(p_{f,a}^m - p_{f,a}^{m-1}\right) = -L_i^{m-1}, \quad \text{otherwise, if } p_{f,a}^m \le 0 \text{ then } p_{f,a}^m = 0. \tag{B.4}$$

Observe that (B.4) cannot be solved with direct methods (a simple matrix inversion does not account for the cavitation condition, that is, it will solve a fluid equation that is not valid in all the domain). For this reason, the domain is divided into two zones, namely a high fluid pressure zone C_1 and a cavitation zone C_2.

Equation (B.4) is computationally simplified by considering the singularity of the elastic kernel,

$$-L_i^{m-1} = \sum_a \frac{\partial L_i^{m-1}}{\partial p_{f,a}}\left(p_{f,a}^m - p_{f,a}^{m-1}\right), \quad a \in [i-2, i+2], \quad i \in C_1, \tag{B.5}$$

and

$$-L_i^{m-1} = \frac{\partial L_i^{m-1}}{\partial p_{f,i}^{m-1}}\left(p_{f,i}^m - p_{f,i}^{m-1}\right), \quad i \in C_2. \tag{B.6}$$

A SUR is applied at the end of the relaxation sweep, with relaxation factor of order 0.1.

The CSU updates the central separation

$$\Delta \bar{u}_0^m = -\alpha_c \Delta F^m \quad \text{if} \quad \Delta F_c^m \cdot \Delta F^m \ge 0, \qquad \Delta \bar{u}_0^m = 0 \quad \text{otherwise}, \tag{B.7}$$

where

$$\Delta F^m = F_{\rm N}/L - \delta_x \sum_i p_i^m,$$
$$\Delta F_c^m = \sum_i p_i^m - \sum_i p_i^{m-1},$$

and where α_c is in the range 10^{-2} to 1 (*e.g.*, α_c can be put equal to $\bar{u}_0^{n-1}/(F_{\rm N}/L)$ when starting from a previous velocity step solution). Equation (B.7), without the logical condition, is widely used by the EHL community to close the system of equations. However, the inequality condition introduces a *logical damping* into the convergence history of the contact solutions, and this has been shown to largely improve the convergence speed of the calculation [32].

After the update of the central separation, the shape of the contact is determined by solving the coupled elastic and solid contact equations as a Fredholm type of integral equation. The FS solves the latter by a NR method. Considering that $\bar{u}_i > 0$, (B.1) can be rewritten as

$$0 = g_i = -1 + \frac{\bar{u}_0 + f_i + \sum_h \left(D_i^h - D_0^h\right)\left[p_{f,h} + p_s\left(\bar{u}_h\right)\right]}{\bar{u}_i}. \tag{B.8}$$

By considering the form of the elastic kernel, the Jacobian **J** can be approximated

$$[\mathbf{J}]_i^l \approx \delta_i^l \frac{\partial g_i}{\partial \bar{u}_l}$$

and so

$$\bar{u}_i^l = \bar{u}_i^{l-1}\left[1 + \alpha_{\mathrm{fs}} \frac{g_i^{l-1}}{1 + g_i^{l-1} - \left(D_0^0 - D_0^i\right)\left[\frac{\partial p_s}{\partial \bar{u}}\right]_{\bar{u}_i^{l-1}}}\right], \quad i \neq 0,$$

where α_{fs} is generally between 0.1 to 1 (the higher value for the hydrodynamic region, where $g_i^n \to 0$). In our calculations, a target convergence error for fluid pressure field is 5×10^{-7}, with an average g_i of 10^{-6}. After the update of separation, the loop restarts from RSA.

References

1. N. Patir, H.S. Cheng, J. Tribol. Trans. ASME **100**, 12 (1978).
2. N. Patir, H.S. Cheng, J. Tribol. Trans. ASME **101**, 220 (1979).
3. J.A. Greenwood, J.B.P. Williamson, Proc. R. Soc. London, Ser. A **295**, 300 (1966).
4. A.W. Bush, R.D. Gibson, T.R. Thomas, Wear **35**, 87 (1975).
5. B.N.J. Persson, J. Phys.: Condens. Matter **20**, 312001 (2008).
6. C. Campana, M.H. Müser, M.O. Robbins, J. Phys.: Condens. Matter **20**, 354013 (2008).
7. B.N.J. Persson, Phys. Rev. Lett. **99**, 125502 (2007).
8. C. Yang, B.N.J. Persson, J. Phys.: Condens. Matter **20**, 215214 (2008).
9. B. Lorenz, B.N.J. Persson, J. Phys.: Condens. Matter **201**, 015003 (2009).
10. F. Sahlin, A. Almqvist, R. Larsson, S. Glavatskih, Tribol. Int. **40**, 1025 (2007).
11. A. Almqvist, E.K. Essel, J. Fabricius, P. Wall, Proc. Inst. Mech. Engin., Part J: J. Engin. Tribol. **222**, 827 (2008).
12. S.R Harp, R.F. Salant, ASME J. Tribol. **123**, 134 (2001).
13. J.H. Tripp, ASME J. Lubrication Technol. **105**, 485 (1983).
14. B.N.J. Persson, J. Phys.: Condens. Matter **22**, 265004 (2010).
15. M. Scaraggi, B.N.J. Persson, G. Carbone, D. Dini, Soft Matter, DOI: 10.1039/c1sm05128h.
16. M. Scaraggi, G. Carbone, D. Dini, Soft Matter, DOI: 10.1039/c1sm05129f.
17. B.N.J. Persson, C. Yang, J. Phys.: Condens. Matter **20**, 315011 (2008).
18. See, *e.g.*, B.N.J. Persson, O. Albohr, U. Tartaglino, A.I. Volokitin, E. Tosatti, J. Phys.: Condens. Matter **17**, R1 (2005).
19. D. Bruggeman, Ann. Phys. (Leipzig) **24**, 636 (1935).
20. S. Kirkpatrick, Rev. Mod. Phys. **45**, 574 (1973).
21. M. Sahimi, *Heterogeneous Materials I* (Springer, New York, 2003).
22. B. Lorenz, B.N.J. Persson, Eur. Phys. J. E **31**, 159 (2010).
23. A. Almqvist, C. Campañá, N. Prodanov, B.N.J. Persson, J. Mech. Phys. Solids **59**, 2355 (2011).
24. H. Eyring, J. Chem. Phys. **4**, 283 (1936).
25. B.N.J. Persson, *Sliding Friction: Physical Principles and Applications* 2nd edn. (Springer, Heidelberg, 2000).
26. S. Yamada, Tribol. Lett. **13**, 167 (2002).
27. L. Bureau, Phys. Rev. Lett. **104**, 218302 (2010).
28. P.A. Thompson, G.S. Grest, M.O. Robbins, Phys. Rev. Lett. **68**, 3448 (1992).
29. I.M. Sivebaek, V.N. Samoilov, B.N.J. Persson, subm. to PRL.
30. B.N.J. Persson, F. Mugele, J. Phys.: Condens. Matter **16**, R295 (2004).
31. S. Bair, *High Pressure Rheology for Quantitative Elastohydrodynamics* (Elsevier, 2007).
32. B.N.J. Persson, M. Scaraggi, J. Phys.: Condens. Matter **21**, 185002 (2009).
33. K.L. Johnson, *Contact Mechanics* (Cambridge University Press, Cambridge, 1985).
34. B.N.J. Persson, J. Chem. Phys. **115**, 3840 (2001).
35. B.N.J. Persson, Surf. Sci. Rep. **61**, 201 (2006).
36. M. Scaraggi, G. Carbone, D. Dini, Tribol. Lett. **43**, 169 (2011).
37. Nestor Rodriguez, private communication.
38. J. Israelachvili, private communication.